

Scale Setting and Strong Coupling Determination in the Gradient Flow Scheme for 2+1 Flavor Lattice QCD

Rasmus Norman Larsen^a Swagato Mukherjee^b Peter Petreczky^b Hai-Tao Shu^c
Johannes Heinrich Weber^{d,f}

^a*Fakultät für Physik, Universität Bielefeld, D-33615 Bielefeld, Germany*

^b*Physics Department, Brookhaven National Laboratory, Upton, New York 11973, USA*

^c*Key Laboratory of Quark & Lepton Physics (MOE) and Institute of Particle Physics, Central China Normal University, Wuhan 430079, China*

^d*Institut für Physik & IRIS Adlershof, Humboldt-Universität zu Berlin, D-12489 Berlin, Germany*

^f*Institut für Kernphysik, Technische Universität Darmstadt, Schlossgartenstraße 2, D-64289 Darmstadt, Germany*

E-mail: hai-tao.shu@ccnu.edu.cn

ABSTRACT: We report on the determination of the gradient flow scales in $N_f = 2 + 1$ QCD using highly improved staggered quark (HISQ) ensembles generated by the HotQCD Collaboration for bare gauge couplings ranging from $\beta = 6.423$ to 8.400. Using bottomonium splittings, kaon decay constant, the decay constant of unmixed η_s meson and the ϕ meson mass we obtained the values of the gradient flow scales in physical units, $\sqrt{t_0} = 0.14428(48)$ fm and $w_0 = 0.17391(52)$ fm. Using the same physical inputs we revisit the determination of the potential r_1 scale and find $r_1 = 0.3112(24)$ fm. As a byproduct of our study we obtain the running of the gauge coupling in the gradient flow scheme. We find that within the uncertainties the running of the gradient flow coupling obtained on the lattice is compatible with the perturbative results up to flow radius $\sqrt{8\tau_F} = 0.15$ fm.

Contents

1	Introduction	1	4.2	Determination of the theory scales from decay constants	15
2	Formalism	3	4.3	Scale determination through the ϕ meson mass	17
3	Gradient flow scales in 2+1 flavor lattice QCD	5	4.4	Final values of the theory scales	18
3.1	Lattice setup	5	5	Gradient flow coupling	21
3.2	Determination of the gradient flow scales	6	6	Conclusions	24
3.3	The relation of the gradient flow scales to the potential scales	10	A	Gradient flow scales computed on the finite lattices	25
4	Gradient flow scales in physical units	13	B	Influence of topological freezing and the light quark mass on flow observables	25
4.1	Determination of the theory scales from bottomonium mass splitting	14			

1 Introduction

Scale setting is an essential step in the lattice calculations that converts the lattice computed dimensionless quantity to dimensionful quantity in physical units. It affects the accuracy of lattice calculations in such a fundamental way that it must be handled as precisely as possible. There are different strategies to this end, which roughly divide into two categories. One is to use the physical scales that are experimentally accessible, the other is to use the theory scales. The former mainly includes the masses of baryons (e.g. Ω) [1–5] and the pion/kaon decay constant f_π/f_K , see, e.g. [1, 4–6]. The latter mainly includes the (static-quark) potential scales r_0 and r_1 [7–12], the decay constant F_{p4s} of fictitious pseudo-scalar meson with mass 0.4 times the strange quark mass [13, 14], and the gradient flow scales t_0 and w_0 [1–3, 3, 10, 14–19] which we will pursue in this work. Calculating theory scales on the lattice is often much easier than calculating physical quantities and therefore, these are useful to determine the lattice spacing in practical lattice QCD calculations. One prominent example is calculation at nonzero temperature, which often requires simulations at many lattice spacings. Because the theory scales themselves have no direct physical meaning, their ratios to physical observables must first be determined at each lattice spacing. These ratios are then extrapolated to the continuum limit, from which the theory scale in physical units is obtained. In principle, any dimensionful quantity can be used to “define” a theory scale,

as long as it is finite in the continuum limit. But in practice it is only worth to consider those that are cheap and straightforward to compute on the lattice. That is, these quantities must be precise enough that with a small computational cost one can acquire good control on the statistical and systematic uncertainties.

Among them are the commonly used potential scales r_0 and r_1 proposed decades ago [7, 8]. They are defined by $r^2 dV(r)/dr = 1.65$ or 1 for $r = r_0$ or r_1 , respectively. Usually the potential $V(r)$ itself is precise on the lattice, but when the lattice is very fine, the statistical uncertainties of the Wilson loops at large temporal distances (in lattice units) become significant, which weakens the control of the excited-state contamination. F_{p4s} , on the other hand, has a relatively strong dependence on the valence quark mass. To obtain F_{p4s} one needs to perform fits to meson correlation function at asymptotically large separations, which again could be challenging for small lattice spacing.

Gradient flow [20, 21] is a seminal framework that has applications in many fields, such as renormalization, defining operators, noise reduction, scale setting *etc.* The flow scales are introduced based on a crucial property of gradient flow that it renormalizes composite operators at positive finite flow time [22]. For gradient flow scales the relevant composite operator is the vacuum gauge action density E . The flow scales have been a topic of intense study for the last decade for their stability and high precision. This is due to the fact that the action density is very precise on the lattice and no fits of correlation functions at large separations are needed.

The gradient flow scales t_0 and w_0 are the most commonly used at present. Therefore, it is important to obtain precise and reliable results for them. Cross comparison of different lattice QCD calculations of t_0 and w_0 can help to reach this goal. The number of independent determination of these scales in 2+1+1 flavor QCD is limited because several determinations use the same set of gauge configurations. There is some tension between the determination of the t_0 and w_0 scale obtained using rooted staggered fermions [2, 14, 18, 23] and twisted mass fermions [15]. For 2+1 flavor QCD the Flavor Lattice Averaging Group (FLAG) quotes a t_0 value with very small error in their 2024 report. However, there is a significant scattering in different t_0 determination that enter the FLAG 2024 report [24]. Calculating both w_0 and t_0 as well as their ratio could provide an important consistency check. However, many studies present only results on either t_0 or w_0 . Furthermore, it may be also interesting to study the ratio of gradient flow scales and the potential scales. Unfortunately, very few studies are available for such ratios. An interesting question is whether the gradient flow scales are different in 2+1 flavor and 2+1+1 flavor QCD. The FLAG report tends to suggest that this is the case [24], but the calculation by ETMC in 2+1+1 flavor QCD with twisted mass Wilson fermions arrives at the opposite conclusion [15].

The goal of this work is to determine the gradient flow scales t_0 and w_0 as well as their ratio to the r_1 scale in 2+1 flavor QCD using the HISQ action and the gauge configurations generated at many different lattice spacings [10, 25, 26]. One of the motivations of this study is scale setting for calculations at high temperature in 2+1 flavor QCD with HISQ action [27–34]. In these calculations the scale was almost exclusively fixed by r_1 . It would be good to have an alternative way for determining the scale for these calculations.

There are not many independent determinations of the r_1 scale as many of the existing

determinations use the same set of rooted staggered gauge configurations. There is tension between some of the determinations, including the recent TUMQCD determination [12]. On the other hand the very recent analysis with clover fermion formulation [35] finds that r_1 is in perfect agreement with the FLAG average. Therefore, we also revisit the determination of r_1 scale in this work and compare it with the very recent result from Ref. [35].

The gradient flow also allows to define a running coupling constant in QCD. It has been suggested that calculating the running coupling constant in gradient flow scheme and then converting the results to $\overline{\text{MS}}$ scheme could be a viable way to determine the QCD Λ parameter [36, 37]. Therefore, in this work we will also calculate the gradient flow coupling in the continuum limit at small flow time.

This paper is organized as follows. We start with a short summary of the theoretical foundations, including the gradient flow equations, the definitions of the gradient flow scales and the Allton-type ansatz that relates the flow scales to β in Sec. 2. In Sec. 3.1 we provide the lattice setup used in this study. In Sec. 3.2 we present our results for the flow scales, the comparisons of the ratios of scales with the literature and the relation that determines the lattice spacing a given β via flow scales. In Sec. 4 we present the results for the flow scales and potential scales in physical units. In Sec. 5 we discuss the QCD running coupling constant in the gradient flow scheme in the continuum limit and comparison with the perturbative running. We summarize our findings in Sec. 6.

2 Formalism

Yang-Mills gradient flow evolves the gauge fields along the gradient of the gauge action according to the following diffusion equations [20, 21]

$$B_\mu(x, \tau_F = 0) = A_\mu(x), \quad (2.1)$$

$$\partial_{\tau_F} B_\mu(x, \tau_F) = D_\nu G_{\nu\mu}, \quad (2.2)$$

where $A_\mu(x)$ is the original gauge field and $B_\mu(x, \tau_F)$ denotes the gauge field flowed to flow time τ_F . D_ν and $G_{\nu\mu}(x)$ are the flowed covariant derivative and field strength constructed using $B_\mu(x, \tau_F)$. On the lattice the flow equations take the form

$$V(x, \mu)|_{\tau_F=0} = U(x, \mu), \quad (2.3)$$

$$\frac{d}{d\tau_F} V(x, \mu) = -g_0^2 \{ \partial_{x,\mu} S_G(V) \} V(x, \mu), \quad (2.4)$$

where $U(x, \mu)$ is the original gauge link and $V(x, \mu)$ is its flowed version. g_0 is the bare coupling and S_G can take different forms upon how the gauge action is discretized. In this work we use the *Zeuthen flow* [38] that adopts a Symanzik improved Lüscher–Weisz gauge action [39, 40] eliminating tree-level $\mathcal{O}(a^2)$ discretization effects [38].

The leading-order solutions of the flow equations in Eq. (2.1) can be expressed in terms

of a τ_F -dependent transformation of the gauge field $B_\mu(x, \tau_F)$ [41]:

$$\begin{aligned} B_\mu(x, \tau_F) &= \int d^4y K_{\tau_F}(x-y) A_\mu(y), \\ K_{\tau_F}(z) &= \int \frac{d^4p}{(2\pi)^4} e^{ipz} e^{-\tau_F p^2} = \frac{e^{-z^2/(4\tau_F)}}{(4\pi\tau_F)^2}, \end{aligned} \quad (2.5)$$

where K_{τ_F} is a local Gaussian smearing kernel with radius $\sqrt{8\tau_F}$ [22]. The smearing removes the short-distance fluctuations of the gauge fields and has been widely used as a noise reduction technique, see e.g. [42–45]. In this work we use it to define non-perturbative reference scales, which involve a very simple gauge invariant operator, the action density, that reads

$$E(\tau_F, x) = -\frac{1}{2} \text{Tr}\{G_{\mu\nu}(\tau_F, x)G_{\mu\nu}(\tau_F, x)\}. \quad (2.6)$$

In practical simulations an average over all space-time position x is taken.

The gradient flow scales t_i and w_i can be defined by imposing the conditions [3, 41]

$$\begin{aligned} \tau_F^2 \langle E(\tau_F) \rangle \Big|_{\tau_F=t_i} &= c_i, \\ \tau_F \frac{d}{d\tau_F} \{ \tau_F^2 \langle E(\tau_F) \rangle \} \Big|_{\tau_F=w_i^2} &= c_i, \quad i = 0, 1, 2. \end{aligned} \quad (2.7)$$

The commonly used choice $c_0 = 0.3$ defines the scales t_0 and w_0 that are often used in the lattice calculations. The alternative choice $c_1 = 0.7$ has been used by Wuppertal-Budapest Collaboration to define w_1 scale [46]. In this work we also consider the choice $c_2 = 0.2$ that defines scales t_2 and w_2 . Note that in lattice calculations all quantities are in lattice units, thus what one can obtain from these two conditions are actually two dimensionless quantities $\sqrt{t_i}/a$ and w_i/a . In this study, we consider two different discretizations for the action density E , in terms of two different discretization for the field strength tensor $G_{\mu\nu}$. One is to use the clover-type discretization

$$\hat{G}_{\mu\nu}^{\text{clo}}(n) = -\frac{i}{8} \left(Q_{\mu\nu}(n) - Q_{\nu\mu}(n) \right), \quad (2.8)$$

where $Q_{\mu\nu}(n)$ is sum of four square plaquettes, see, e.g. Ref. [47]. The operator is hatted to indicate that it is in lattice units. The other is based on an a^2 -improved discretization that employs a mixture of square and 1×2 rectangle plaquettes

$$\hat{G}_{\mu\nu}^{\text{imp}}(n) = \frac{5}{3} C_{\mu\nu}^{(1,1)}(n) - \frac{1}{3} C_{\mu\nu}^{(1,2)}(n), \quad (2.9)$$

see e.g. Ref. [48] for more details. The use of two different discretization schemes for the action density provides important consistency checks in the determination of the gradient flow scales as will be explained below.

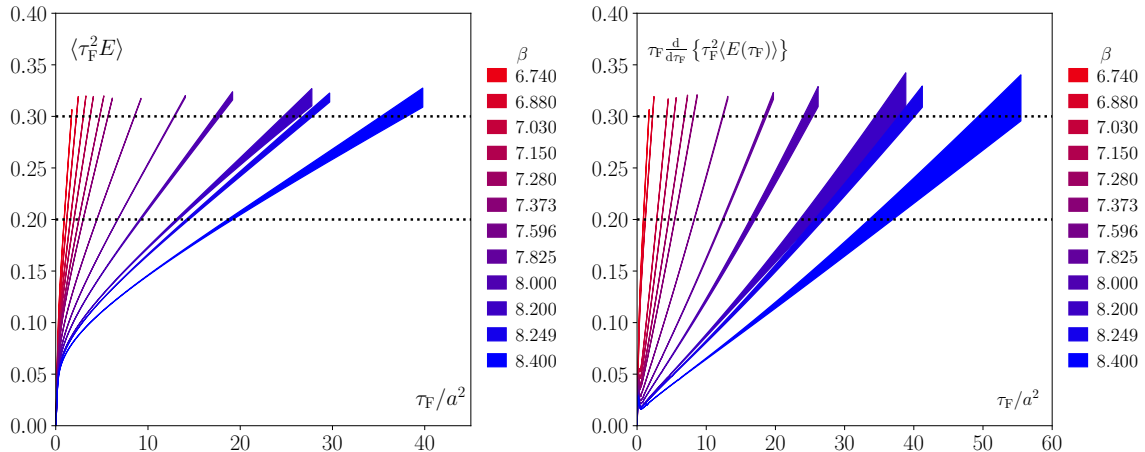


Figure 1. Numerical results for the action density, E (left) and the derivative of $\tau_F^2 E$ (right) as function of the flow time obtained using the improved discretization.

Once the flow scales are obtained, they are fitted to the following Allton-type Ansatz [49] as a function of β

$$\begin{aligned}
 \frac{\sqrt{t_i}}{a} &= \frac{1 + d_{2i}(10/\beta)f^2(\beta)}{c_{0i}f(\beta) + c_{2i}(10/\beta)f^3(\beta)}, \\
 \frac{w_i}{a} &= \frac{1 + d'_{2i}(10/\beta)f^2(\beta)}{c'_{0i}f(\beta) + c'_{2i}(10/\beta)f^3(\beta)}, \\
 f(\beta) &= \left(\frac{10b_0}{\beta}\right)^{-b_1/(2b_0^2)} \exp(-\beta/(20b_0)),
 \end{aligned} \tag{2.10}$$

where $\beta = 10/g_0^2$, $b_0 = 9/(4\pi)^2$ and $b_1 = 1/(4\pi^4)$ for $N_f = 3$. (d_{2i} , c_{0i} , c_{2i}) and (d'_{2i} , c'_{0i} , c'_{2i}) are fit parameters. Using t_0 and w_0 in physical units obtained through , e.g. bottomonium mass splitting, the lattice spacing can be predicted for a new β .

3 Gradient flow scales in 2+1 flavor lattice QCD

3.1 Lattice setup

The calculations are carried out on the ensembles generated by the HotQCD Collaboration in Refs. [10, 25, 26] using 2+1 flavor HISQ action [50] and tree-level improved Lüscher-Weisz gauge action [39, 40]. Seventeen different values of the lattice gauge coupling $\beta = 10/g_0^2$ are employed in this study, ranging from 6.423 to 8.400. The calculations have been performed for the strange quark mass, m_s close to its physical value, while the degenerate light quark masses were fixed to be either $m_s/m_l = 20$ or $m_s/m_l = 5$. For the largest β value additional gauge configurations have been generated to improve the determinations of the gradient flow scales. The details are summarized in Tab. 1. In the first block of Tab. 1 ($6.423 \leq \beta \leq 7.825$), the light quark masses are fixed as a fraction of the strange quark mass $m_s/m_l = 20$, slightly above the physical ratio $m_s/m_l = 27.3$. This corresponds to a pion mass of about 160 MeV in the continuum limit. The second block corresponds to the light quark mass of $m_s/m_l = 5$

β	am_s	am_l	N_σ	N_τ	# conf.
6.423	0.0670	0.00335	32	32	500
6.515	0.0604	0.00302	32	32	500
6.550	0.0582	0.00291	32	32	700
6.575	0.0564	0.00282	32	32	500
6.664	0.0514	0.00257	32	32	700
6.740	0.0476	0.00238	48	48	700
6.880	0.0412	0.00206	48	48	627
7.030	0.0356	0.00178	48	48	900
7.150	0.0320	0.00160	48	64	395
7.280	0.0280	0.00142	48	64	398
7.373	0.0250	0.00125	48	64	554
7.596	0.0202	0.00101	64	64	577
7.825	0.0164	0.0082	64	64	471
7.030	0.0356	0.00712	48	48	280
7.825	0.01542	0.003084	64	64	160
8.000	0.01299	0.002598	64	64	1004
8.200	0.01071	0.002142	64	64	961
8.249	0.01011	0.002022	64	64	2241
8.400	0.00887	0.001774	64	64	2372

Table 1. Parameters of the lattice ensembles used in this work, including the inverse gauge coupling $\beta = 10/g_0^2$, the bare quark masses in lattice units, the spatial and temporal lattice extent N_σ and N_τ , and the corresponding number of configurations.

and $7.030 \leq \beta \leq 8.400$. This light quark mass is equivalent to the pion mass of about 320 MeV in the continuum limit. These gauge configurations have been used as the zero temperature reference for the calculations at high temperature [25, 26, 32] as well as for the determination of the heavy quark masses and strong coupling constant through the moments of quarkonium correlators [51, 52]. As discussed in Ref. [25] the generated gauge configurations for $\beta = 8.0, 8.2$ and 8.4 are at fixed topology for a given Monte-Carlo stream. However, we have streams that belong to different values of topological charge [25] allowing us to estimate the effects of frozen topology for the quantities of interest as discussed below.

3.2 Determination of the gradient flow scales

We determine the gradient flow scales t_i and w_i , $i = 0, 2$ through Eq. (2.7) using clover or improved discretization for the action density. The numerical results for the action density, E and the derivative of $\tau_F E$ as function of the flow time are shown in Fig. 1 for improved discretizations. The results for clover discretization look similar. We interpolate the numerical results on the action density in flow time using splines. From the splines it is straightforward to estimate the derivative of $\tau_F E$ as well as to evaluate the gradient flow scales. Our results for the gradient flow scales in lattice units are summarized in Tab. 6 and 7 in Appendix A. The t_2 and w_2 scales have smaller statistical errors compared to t_0 and

	c_{00}	$c_{20}/10^5$	$d_{20}/10^3$	$\chi^2/\text{d.o.f.}$
$\sqrt{t_0}/a$	93.2767(0.0747)	5.9633(0.1149)	3.9169(0.0975)	9.8
	c'_{00}	$c'_{20}/10^5$	$d'_{20}/10^3$	$\chi^2/\text{d.o.f.}$
w_0/a	78.0681(0.1204)	2.9399(0.1236)	1.5429(0.1191)	22.2
	c_{00}	$c_{20}/10^6$	$d_{20}/10^4$	$\chi^2/\text{d.o.f.}$
$\sqrt{t_0}/a$	88.2315(1.6795)	4.4900(1.7799)	4.0278(1.6889)	0.5
	c'_{00}	$c'_{20}/10^6$	$d'_{20}/10^4$	$\chi^2/\text{d.o.f.}$
w_0/a	74.6393(2.8458)	2.4417(2.3542)	2.4608(2.6035)	0.5

Table 2. Fit parameters of the gradient flow scales obtained from the improved discretization to the Allton Ansatz. Here we rescale the fit parameters to make the values more readable. We only consider the improved discretization. The top block is for the $m_s/m_l = 20$ ensembles while the bottom block is for the $m_s/m_l = 5$ ensembles.

	$\frac{\sqrt{t_0}/w_0}{a^2}$	$\frac{\sqrt{t_2}/w_2}{a^2}$	$\frac{\sqrt{t_0}/\sqrt{t_2}}{a^2}$	$\frac{w_0/w_2}{a^2}$		
8 largest β	0.8390(7), 3.0	0.7562(7), 22.0	1.3580(5), 42.0	1.2302(9), 2.8		
7 largest β	0.8351(14), 1.6	0.7478(10), 6.7	1.3657(7), 15.6	1.2268(15), 1.5		
6 largest β	0.8337(19), 1.3	0.7426(15), 2.6	1.3717(10), 4.9	1.2256(20), 1.4		
5 largest β	0.8307(28), 1.0	0.7382(20), 1.1	1.3762(14), 1.6	1.2244(28), 1.5		
4 largest β	0.8318(44), 1.0	0.7357(32), 0.8	1.3799(22), 0.5	1.2202(40), 1.1		
3 largest β	0.8331(49), 0.9	0.7369(38), 0.5	1.3792(27), 0.3	1.2194(47), 1.0		
	$\frac{\sqrt{t_0}/w_0}{a^2}$	$\frac{\sqrt{t_2}/w_2}{a^4}$	$\frac{\sqrt{t_0}/\sqrt{t_2}}{a^2}$	$\frac{w_0/w_2}{a^4}$	$\frac{\alpha_b a^2}{a^2}$	
8 largest β	0.8275(7), 1.2	0.8331(5), 1.5	0.8289(7), 1.1	0.7302(7), 1.3	0.7388(5), 7.0	0.7323(6), 1.7
7 largest β	0.8285(12), 1.0	0.8325(7), 1.3	0.8294(11), 1.0	0.7297(9), 1.3	0.7364(6), 3.2	0.7314(8), 1.5
6 largest β	0.8286(20), 1.0	0.8315(13), 1.2	0.8293(19), 1.1	0.7285(13), 1.3	0.7345(9), 1.8	0.7299(13), 1.3
5 largest β	0.8262(32), 0.9	0.8296(20), 0.8	0.8269(30), 0.9	0.7264(19), 1.2	0.7325(11), 1.0	0.7277(18), 1.1
4 largest β	0.8276(47), 1.0	0.8295(28), 0.9	0.8280(43), 1.0	0.7274(37), 1.4	0.7311(22), 0.9	0.7282(34), 1.3
3 largest β	0.8291(64), 1.1	0.8301(40), 1.1	0.8293(59), 1.1	0.7311(40), 0.5	0.7331(27), 0.4	0.7316(37), 0.4
	$\frac{\sqrt{t_0}/\sqrt{t_2}}{a^2}$	$\frac{\sqrt{t_0}/\sqrt{t_2}}{a^4}$	$\frac{\alpha_b a^2}{a^2}$	$\frac{w_0/w_2}{a^2}$	$\frac{w_0/w_2}{a^4}$	$\frac{\alpha_b a^2}{a^2}$
8 largest β	1.3869(5), 2.2	1.3794(3), 10.4	1.3850(5), 2.9	1.2249(9), 1.1	1.2247(6), 1.1	1.2248(8), 1.1
7 largest β	1.3874(7), 2.3	1.3812(5), 6.0	1.3859(7), 2.7	1.2239(15), 1.0	1.2242(9), 1.0	1.2240(13), 1.0
6 largest β	1.3888(11), 1.9	1.3834(7), 3.4	1.3876(11), 2.1	1.2235(22), 1.0	1.2238(14), 1.0	1.2236(20), 1.0
5 largest β	1.3906(17), 1.5	1.3854(10), 1.5	1.3894(15), 1.5	1.2241(33), 1.0	1.2243(20), 1.0	1.2242(30), 1.0
4 largest β	1.3907(26), 1.8	1.3870(17), 1.1	1.3899(23), 1.7	1.2220(46), 0.9	1.2229(28), 1.0	1.2222(41), 1.0
3 largest β	1.3880(32), 0.6	1.3859(22), 0.4	1.3875(30), 0.5	1.2236(69), 1.1	1.2240(40), 1.1	1.2237(62), 1.1

Table 3. Continuum-extrapolated ratios of the flow scales from different fit strategies using data from the clover (top) and improved discretization (middle and bottom). The numbers are in the form {Mean(Error), $\chi^2/\text{d.o.f.}$ }.

w_0 scales, which is advantageous for large values of β . For $\beta \geq 6.74$ the gradient flow scales are determined for both clover and improved discretization. There are differences between the gradient flow scales obtained using clover and improved discretizations schemes. These

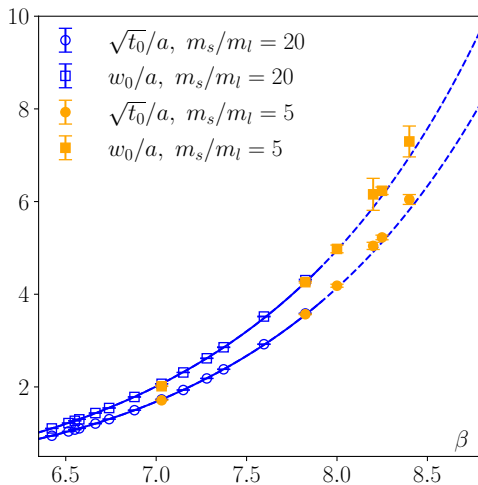


Figure 2. The gradient flow scales $\sqrt{t_0}$ and w_0 obtained from the improved discretization as functions of β . The open points in blue are for the $m_s/m_l = 20$ lattices while the filled points in orange are for the $m_s/m_l = 5$ lattices. The solid lines (means) and bands (errors) represent the fits to Allton Ansatz of the $m_s/m_l = 20$ lattices ($6.423 \leq \beta \leq 7.825$). The dashed lines represent the extrapolation of the fits to the $m_s/m_l = 5$ lattices, to test the robustness of the fit by comparing its extrapolated predictions with data not included in the fitting procedure.

differences are the largest for t_2 and the smallest for w_0 . Furthermore, as expected, the differences between the gradient flow scales obtained using clover and improved discretizations decrease with increasing β .

As mentioned in the previous section, for $\beta \geq 8.0$ the individual Monte-Carlo streams correspond to frozen topology. Fortunately, we have streams that correspond to several values of topological charge. One may hope that the gradient flow scales being short distance quantities, i.e. being determined at relatively small values of the flow time, will not be affected much by the frozen topology. It has been shown that this is the case for the potential scales r_1 and r_2 determined at these values of β [25]. We perform a similar analysis for the gradient flow scale in Appendix B, where we show that the values of the gradient flow scale obtained using Monte-Carlo streams with different values of the topological charge agree within the statistical errors. Thus at present level of statistical accuracy we do not see any effects of topological freezing on the values of the gradient flow scales.

We performed Allton fits of the gradient flow scales $\sqrt{t_0}/a$ and w_0/a obtained from the improved discretization for $m_s/m_l = 20$ and $6.740 \leq \beta \leq 7.825$. The parameters of these fits are summarized in Tab. 2 and shown in Fig. 2. While the $\chi^2/\text{d.o.f.}$ of the fit is large due to the tiny errors on the gradient flow scale, overall the fits capture the β dependence of the scale quite well. We also performed Allton fits for $\sqrt{t_0}/a$ and w_0/a obtained for $m_s/m_l = 5$ with improved discretization. The results of these fits are also shown in Fig. 2 and summarized in Tab. 2.

Next we determine the ratio of different gradient flow scales: $\sqrt{t_0}/w_0$, $\sqrt{t_2}/w_2$, $\sqrt{t_0}/\sqrt{t_2}$

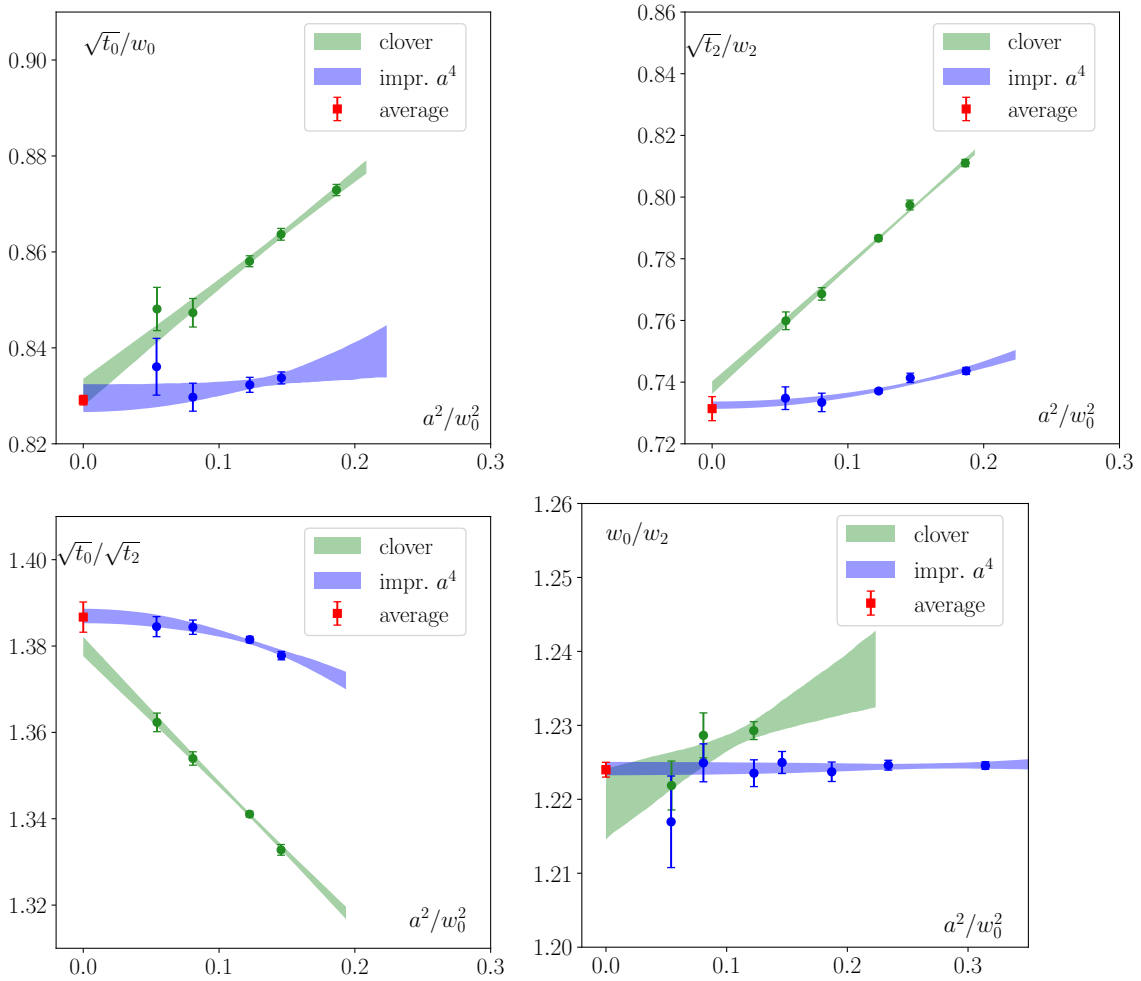


Figure 3. The ratio of different gradient flow scale as function of the lattice spacing together with the continuum extrapolations. The flow scales are measured using both the clover discretizations and the improved discretization (labelled as “clover” and “impr.”, respectively, see Eq. (2.8)-Eq. (2.9)). In these plots only the “best” fits are shown which correspond to the numbers in bold in Tab. 3.

and w_0/w_2 using the same lattices as above. Since these scales are measured on the same ensembles, nontrivial correlations naturally arise among them. To properly account for these correlations, we evaluate each scale separately using the same bootstrap samples. In addition, autocorrelations are present within each measured scale. These are handled by binning the data with a bin size equal to twice the integrated autocorrelation time, τ_{int} , before performing the bootstrap analysis. Here, τ_{int} is taken to be the larger of the values obtained from the numerator and the denominator entering the ratio. These ratios are shown in Fig. 3 as function of the lattice spacing in units of w_0 . As one can see from the figures the results from clover discretization show more pronounced dependence on the lattice spacing compared to the ones from improved discretization. Interestingly, the ratio w_0/w_2 shows very little lattice spacing dependence for improved discretization as can be seen from bottom right panel of Fig. 3.

For clover discretization we expect that these ratios scale as a^2 . For improved discretization we expect the lattice spacing dependence to be proportional to either a^4 or $\alpha_s a^2$. We see that indeed the a^2 dependence of these ratios is much reduced compared to clover discretization. We performed continuum extrapolations of these ratios which are shown as bands in Fig. 3. For clover discretization we performed a^2 extrapolations, while for improved discretization we also performed $\alpha_b a^2$ and a^4 extrapolations, with α_b being the boosted lattice gauge coupling $\alpha_b = g_0^2/(4\pi u_0^4) = 10/(4\pi\beta u_0^4)$. Here u_0^4 stands for the average plaquette taken from [53]. For the improved discretization we also consider the a^2 extrapolations as an effective description of the $\alpha_b a^2$ extrapolations. The continuum-extrapolated results for these ratios show some sensitivity to the choice of the range of lattice spacing used in the fits. Furthermore, the lattice spacing dependence of these ratios may not be described by the above simple forms when the lattice spacing is too large. In addition, the range of lattice spacing that can be used for the continuum extrapolations could be different to clover and improved discretization. To examine the systematic uncertainties stemming from these, we perform the continuum extrapolations by excluding different number of coarser lattices. The fit results are summarized in Tab. 3. We can see that some of the fits can be identified as good while some can not. For the good fits the continuum extrapolated values do not depend on the β range within errors. To pick out the good fits we adopt the following criteria i) $\chi^2/\text{d.o.f.}$ should be the closest to 1.0 (keeping one decimal place); ii) if there are two such fits, we take the one that has more number of data points. The selected best fits are indicated in boldface in Tab. 3. Performing a weighted average of the selected best-fit values, and estimating the systematic uncertainty as the weighted root-mean-square deviation from this average (using the statistical errors as weights), we obtain

$$\begin{aligned}
\sqrt{t_0}/w_0 &= 0.8291(8)(6), \\
\sqrt{t_2}/w_2 &= 0.7314(8)(38), \\
\sqrt{t_0}/\sqrt{t_2} &= 1.3867(10)(34), \\
w_0/w_2 &= 1.2240(7)(7),
\end{aligned}
\tag{3.1}$$

where the first parentheses denote statistical uncertainties and the second denote systematic uncertainties. The averaged results are shown as red data points in Fig. 3, with the error bar being the sum of the statistical uncertainties and the systematic uncertainties in quadrature. The obtained $\sqrt{t_0}/w_0$ is consistent with the $N_f=2+1+1$ estimate from EMT Collaboration [15] 0.82930(65) and the $N_f=2+1+1$ estimate from HPQCD Collaboration [18] 0.835(8).

3.3 The relation of the gradient flow scales to the potential scales

As mentioned in the introduction, theory scales based on the static quark-antiquark potential $V(r)$ are often used in lattice QCD calculations. These scales are defined as

$$r^2 \frac{dV(r)}{dr} \Big|_{r=r_i} = b_i, \quad i = 0, 1, 2.
\tag{3.2}$$

The choices $b_0 = 1.65$, $b_1 = 1$ and $b_2 = 0.5$ define the r_0 (Sommer) [7], r_1 scale [8] and r_2 scale [25], respectively. In this subsection we express the gradient flow scales in terms of

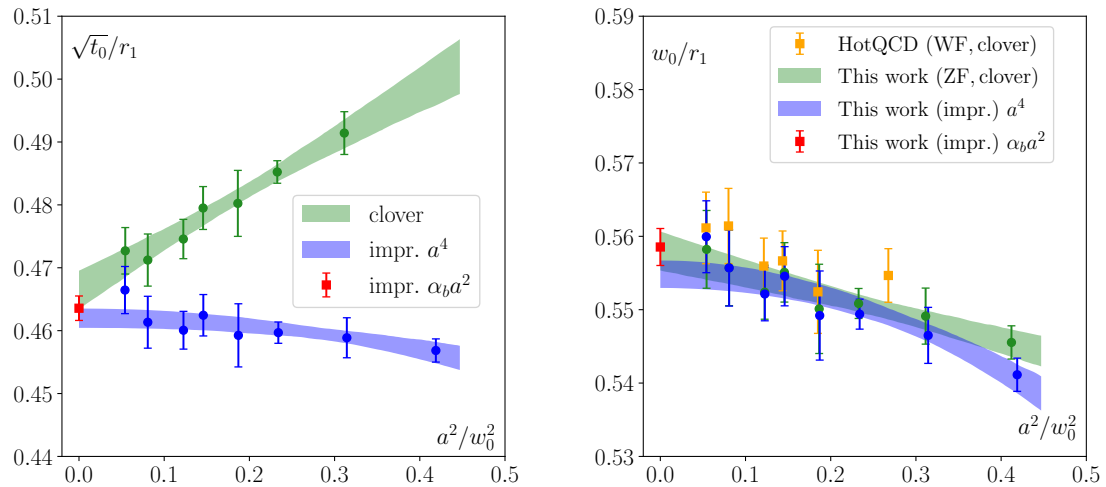


Figure 4. Continuum extrapolation of the ratio of the flow scales to the r_1 scale. Left: $\sqrt{t_0}/r_1$. Similar to before, the discretization effects are significant in this case. After applying the $\mathcal{O}(a^2)$ improvement to the field strength tensor, the slope of the extrapolation (using Ansatz linear in a^2) changes sign. However, in the continuum limit, the two discretizations give consistent results. Right: w_0/r_1 . “WF” stands for Wilson flow and “ZF” for Zeuthen flow. We include results from the HotQCD Collaboration (red points) [10] using Wilson flow and clover-discretized action density for comparison. It can be observed that for w_0 , the discretization effects are so mild that the two discretizations give almost the same results. Our results using Zeuthen flow are slightly smaller than the HotQCD Collaboration’s previous results using Wilson flow.

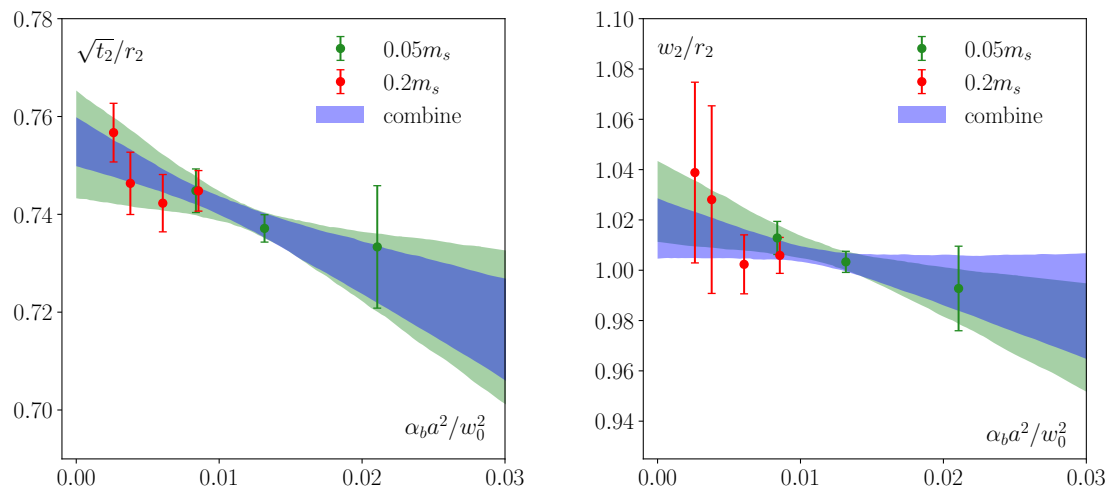


Figure 5. The ratio of the gradient flow scales $\sqrt{t_2}$ and w_2 to r_2 scale as function of the lattice spacing.

r_1 and r_2 scales. Since the discretization effects in the static potential are expected to be small at distances around r_1 and r_2 , the ratio of the gradient flow scales and the potential scales can give some insight into the lattice artifacts in the determination of the gradient flow scales. Based on the $6.740 \leq \beta \leq 7.825$ lattices listed in the first block of Tab. 1, our results for the ratios $r_1/\sqrt{t_0}$ and r_1/w_0 are shown in Fig. 4. For the latter we compare our results with the results of HotQCD Collaboration [10] obtained using Wilson flow and clover-discretized action density for comparison. Our results agree with the HotQCD results within errors. As one can see from the figure of $r_1/\sqrt{t_0}$, improved discretization scheme leads to much smaller cutoff effects. On the other hand for r_1/w_0 there is no visible difference between the two discretization schemes and also Wilson flow leads to similar results. This suggests that lattice artifacts are smaller in the w_0 scale compared to the t_0 scale. We performed continuum extrapolations for $r_1/\sqrt{t_0}$ and r_1/w_0 for both clover and improved discretization assuming a^2 -dependence. For clover discretization we exclude the $\beta = 6.740$ ensemble to gain better fits. For improved action density we also performed $\alpha_b a^2$ and a^4 extrapolations. All the continuum extrapolations of these ratios agree within the estimated errors, see c.f. Fig. 4. Using improved action density and $\alpha_b a^2$ extrapolation we obtain:

$$r_1/\sqrt{t_0} = 2.1572(91), \quad r_1/w_0 = 1.7904(81). \quad (3.3)$$

Our result for r_1/w_0 could be compared with HotQCD result, $r_1/w_0 = 1.7797(67)$ for $N_f = 2 + 1$ [10] and the HPQCD result, $r_1/w_0 = 1.789(26)$ for $N_f = 2 + 1 + 1$ [18]. We see that all results for r_1/w_0 agree within errors. Recently the r_1/a scale has been determined in 2+1+1 flavor QCD using HISQ action by TUMQCD collaboration for physical light quark masses and lattice spacings $a = 0.04, 0.06, 0.09, 0.12$ and 0.15 fm [12]. The gradient flow scales $\sqrt{t_0}/a$ and w_0/a have also been determined on these lattices [14, 23, 54]. In the most recent study also improved discretization for the gauge action density was used to determine w_0 . Using the results on t_0/a from Ref. [54] and the most recent results on w_0/a from Ref. [23] we estimated the continuum values of $r_1/\sqrt{t_0}$ and r_1/w_0 assuming that discretization effects scale as $\alpha_b a^2$:

$$r_1/\sqrt{t_0} = 2.151(10), \quad r_1/w_0 = 1.7713(74), \quad N_f = 2 + 1 + 1. \quad (3.4)$$

Here we have used the values of w_0 and t_0 based on the improved discretization scheme [14]. The resulting value of $r_1/\sqrt{t_0}$ is consistent with our 2+1 flavor determination, whereas the value of r_1/w_0 is slightly smaller than the corresponding 2+1 flavor result.

In Fig. 5 we show the ratio of the gradient flow scales $\sqrt{t_2}$ and w_2 to r_2 . We use data for r_2/a obtained at $\beta = 7.373, 7.596$ and 7.825 , $m_s/m_l = 20$ and $\beta = 7.825, 8.000, 8.200$ and 8.400 for $m_s/m_l = 5$ computed in Ref. [25]. The light quark mass effects in this ratio appear to be quite small. We performed continuum extrapolations for these ratios using $\alpha_b a^2$ form. These continuum extrapolations are shown in Fig. 5 both including and excluding the $m_s/m_l = 5$ lattices. Using all the available data we obtain:

$$\sqrt{t_2}/r_2 = 0.7548(50), \quad w_2/r_2 = 1.0166(120). \quad (3.5)$$

Excluding the $m_s/m_l = 5$ lattices does not change the above result but only increases the errors slightly.

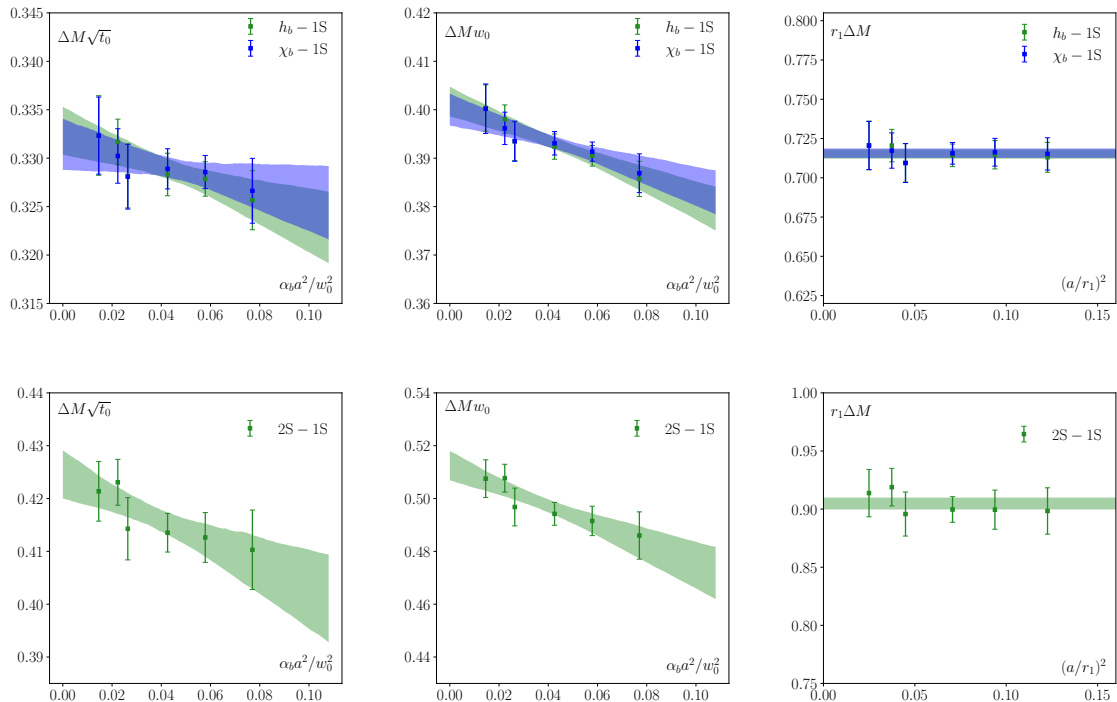


Figure 6. The continuum extrapolation of the products $\Delta M\sqrt{t_0}$ (left), ΔMw_0 (middle) and ΔMr_1 (right) via ΔM_{1P-1S} (top) and ΔM_{2S-1S} (bottom). The mass differences ΔM are taken from Refs. [33, 55]. The bands represent the continuum extrapolation.

4 Gradient flow scales in physical units

To determine the gradient flow scales in physical units, one computes the dimensionless products of these scales with suitable physical quantities such as hadron masses, quarkonium mass splittings, or meson decay constants at several lattice spacings, and extrapolates these products to the continuum limit. Using the experimentally measured values of the corresponding physical quantities, the gradient flow scales can then be expressed in physical units. In the following, we discuss their determination using bottomonium mass splittings, pseudo-scalar meson decay constants, and the ϕ -meson mass.

	$\Delta M\sqrt{t_0}$	ΔMw_0	ΔMr_1	$\sqrt{t_0}$ [fm]	w_0 [fm]	r_1 [fm]
$h_b - 1S$	0.3328(25)	0.4017(31)	0.7151 (30)	0.1446(11)	0.1745(14)	0.3105(14)
$\chi_b - 1S$	0.3314(24)	0.4000(33)	0.7157(30)	0.1438(12)	0.1735(14)	0.3104(13)
$2S - 1S$	0.4245(46)	0.5124(55)	0.9048(51)	0.1465(37)	0.1768(45)	0.3123(75)

Table 4. The continuum-extrapolated values of $\Delta M\sqrt{t_0}$, ΔMw_0 and ΔMr_1 . The physical values of the extracted theory scales $\sqrt{t_0}$, w_0 and r_1 are also provided.

4.1 Determination of the theory scales from bottomonium mass splitting

Bottomonium mass splittings have been used in the determination of the theory scales in the past [6, 56, 57]. In this sub-section we discuss the determination of the theory scales using bottomonium splitting. We use the lattice results on energy levels of different bottomonium states calculated with nonrelativistic QCD (NRQCD) on 2+1 flavor HISQ gauge configurations in Ref. [55] for $\beta = 6.740, 6.880, 7.03, 7.28, 7.596$ and in Ref. [33] for $\beta = 7.373$. In NRQCD absolute value of bottomonium masses are difficult to determine and one usually considers bottomonium mass splittings instead. Since the bottomonium mass differences calculated in NRQCD can be affected by missing higher order relativistic corrections as well as missing radiative corrections to the parameters of NRQCD Lagrangian, it is important to consider mass differences that minimize these effects. The missing corrections in NRQCD Lagrangian mostly affect the mass splittings which are sensitive to spin-spin and spin-orbit interactions. To get rid of the effects of spin-spin interactions we consider the spin averaged 1S and 2S bottomonium masses, $M_{1S} = (M_{\eta_b(1S)} + 3M_{\Upsilon(1S)})/4$ and $M_{2S} = (M_{\eta_b(2S)} + 3M_{\Upsilon(2S)})/4$ and their difference. To minimize the effect to spin-orbit interactions we consider the difference between the mass of $h_b(1P)$ state and M_{1S} as well as the difference between the spin-averaged $\chi_b(1P)$ mass defined as $M_{1P}^{\chi_b} = (1M_{\chi_{b0}(1P)} + 3M_{\chi_{b1}(1P)} + 5M_{\chi_{b2}(1P)})/9$ and M_{1S} . We denote the above mass differences as ΔM with additional labels $2S - 1S$, $h_b - 1S$ and $\chi_b - 1S$.

Similar to previous section, we calculate the dimensionless products $\Delta M\sqrt{t_0}$, ΔMw_0 and $r_1\Delta M$ present on the same ensembles, and then extrapolate them to the continuum limit. The lattice spacing of these dimensionless products are shown in Fig. 6. For the continuum extrapolation of $\Delta M\sqrt{t_0}$ and ΔMw_0 we use an Ansatz linear in $\alpha_b a^2/w_0^2$. Interestingly enough, the combination $r_1\Delta M$ shows no dependence on the lattice spacings within errors, see Fig. 6. Therefore, we fit this combination by a constant. The continuum fits are shown as bands in Fig. 6.

	via f_{η_s}	via f_K	via m_ϕ
$\sqrt{t_0}$ [fm]	0.14354 (17) (95) (21)	0.14443 (39) (65) (35)	0.14461 (43) (6) (67)
w_0 [fm]	0.17315 (40) (114) (46)	0.17425 (40) (78) (15)	0.17389 (51) (7) (59)
r_1 [fm]	0.3105 (37) (21) (7)	0.3131 (37) (14) (1)	0.3122 (31) (1) (10)

Table 5. Theory scales determined via f_{η_s} , f_K and ϕ meson mass. The first error stands for the statistical error. The second error represents the error propagated from the cited decay constants and meson masses. The third error is the systematic error of the continuum extrapolation, which is estimated using the difference between the extrapolated results obtained by including and excluding the coarsest lattice.

Using the values of ΔM taken from PDG [58], we can convert the products to extract the theory scales in physical units. The obtained values of the products and the theory scales are listed in Tab. 4. We note that the mass splittings between different spin-averaged bottomonium states have systematic errors due to the use of NRQCD. The estimates of these errors vary depending on the details of the lattice setup and the states considered and lie between 0.2% \sim 1.2% [18, 59]. We assign a 1% systematic error to the $h_b - 1S$, $\chi_b - 1S$

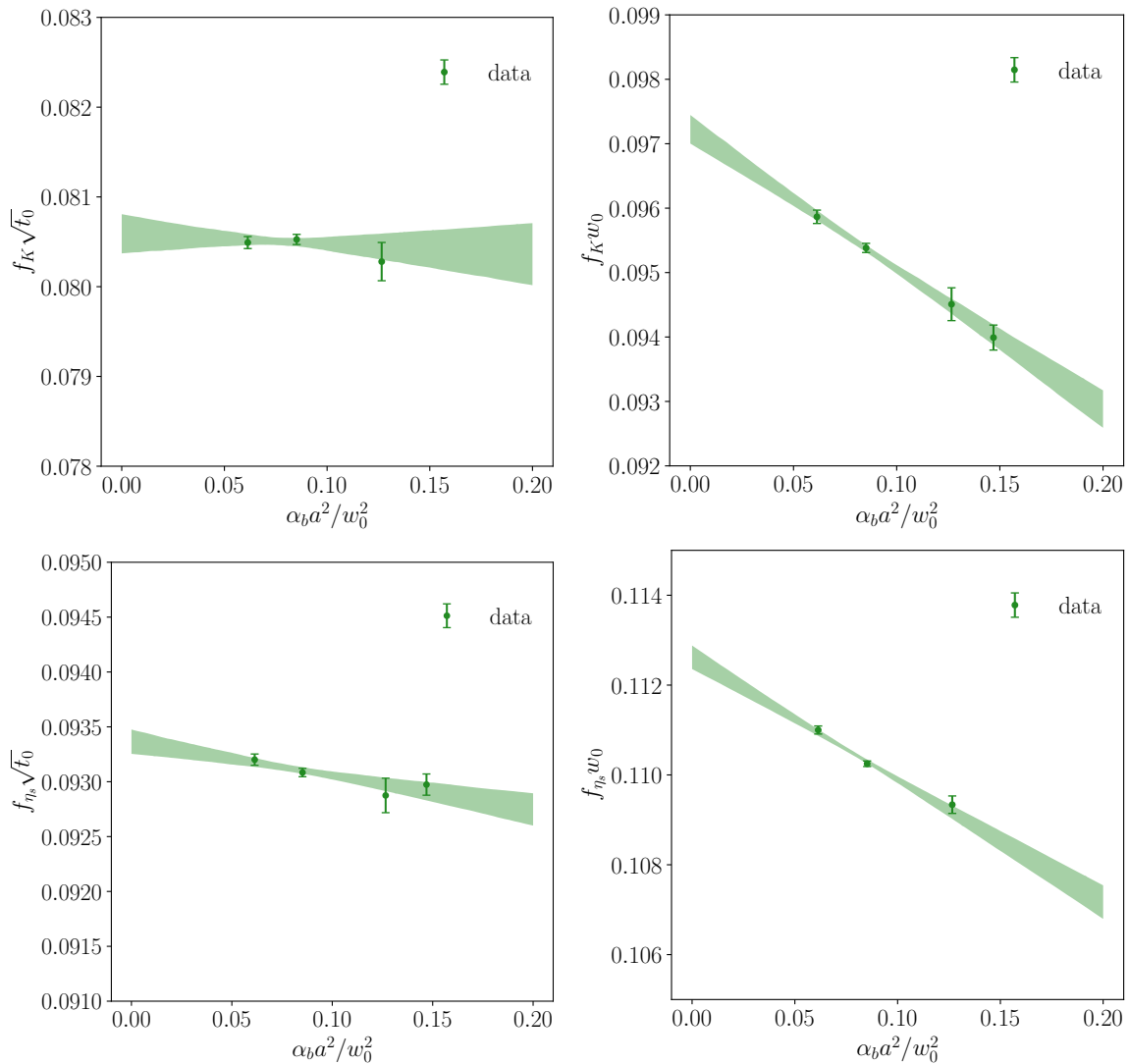


Figure 7. Continuum extrapolation of $\sqrt{t_0}f_K$ (top left), w_0f_K (top right), $\sqrt{t_0}f_{\eta_s}$ (bottom left) and $w_0f_{\eta_s}$ (bottom right) using the $\beta=6.575, 6.740$ and 6.880 lattices.

and $2S - 1S$ splitting and propagate these systematic errors to the corresponding systematic errors on the values of $\sqrt{t_0}$, w_0 and r_1 in physical units. We perform a weighted average of different determinations and add the averaged statistical errors and the 1% systematic errors in quadrature to evaluate a total error and obtain:

$$\begin{aligned}
 \sqrt{t_0} &= 0.14434 (161) \text{ fm}, \\
 w_0 &= 0.17413 (196) \text{ fm}, \\
 r_1 &= 0.3105 (32) \text{ fm}.
 \end{aligned}
 \tag{4.1}$$

4.2 Determination of the theory scales from decay constants

In this section we crosscheck the theory scales determined in the previous section using the kaon decay constant f_K and the decay constant of unmixed pseudo-scalar $s\bar{s}$ meson

f_{η_s} . The decay constant f_{η_s} cannot be determined experimentally as there is no unmixed pseudo-scalar $s\bar{s}$ meson, but the corresponding decay constant can be related to pion and kaon decay constants using chiral perturbation theory [6]. We will use the values of af_K and af_{η_s} obtained by HotQCD Collaboration in 2+1 flavor QCD [10]. The values of f_K and f_{η_s} are very sensitive to the strange quark mass. Unfortunately, the value of the strange quark mass in Ref. [10] does not follow the lines of constant physics well for $\beta > 6.88$. Therefore, here we will only use the pseudo-scalar meson decay constant for $6.515 \leq \beta \leq 6.880$.

Using results of Ref. [10] we form the dimensionless products $f_K w_0$, $f_K \sqrt{t_0}$, $f_{\eta_s} w_0$, $f_{\eta_s} \sqrt{t_0}$, and study their dependence on the lattice spacings. In general, we find that the lattice-spacing dependence of these combinations is significantly reduced when the t_0 and w_0 scales are extracted from the improved gauge-action density. Therefore, in the following analysis we rely exclusively on the gradient flow scales obtained using the improved discretization. We perform continuum extrapolation of these products in $\alpha_b a^2/w_0^2$. Sample continuum extrapolations are shown in Fig. 7. To estimate the systematic errors of the continuum extrapolation we perform continuum fits with and without the data from the coarsest lattice corresponding to $\beta = 6.515$. The difference between these two fits is used as an estimate of the systematic uncertainty.

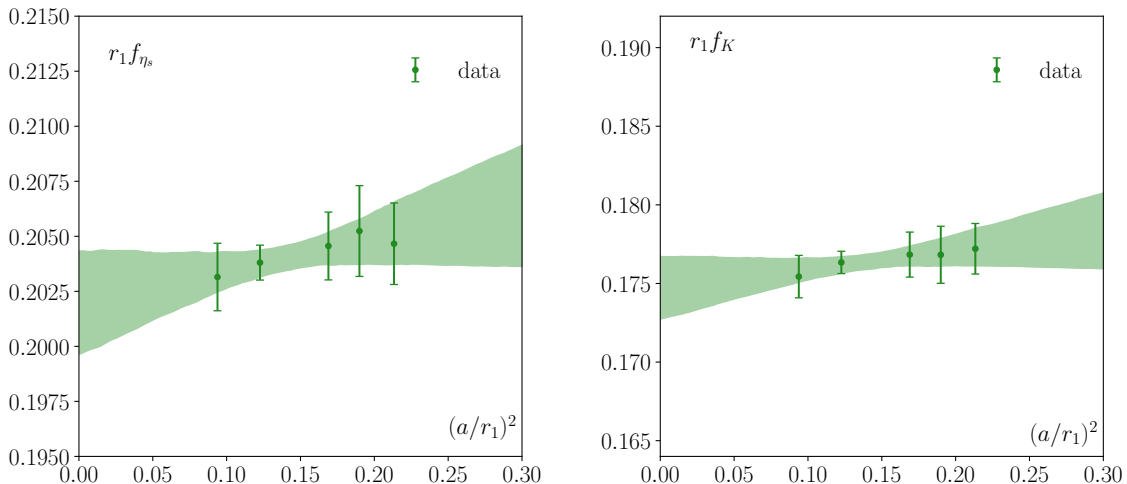


Figure 8. The lattice spacing dependence and continuum extrapolation of $r_1 f_{\eta_s}$ (left) and $r_1 f_K$ (right).

Using the continuum-extrapolated results for the above products together with the values $f_{\eta_s} = 128.34(85)$, MeV [6] and $f_K = 155.7(7)/\sqrt{2}$, MeV [24], we obtain the values of the w_0 and t_0 scales in physical units. These results are presented in Tab. 5, where we indicate the different sources of errors. By combining the statistical uncertainty, the systematic uncertainties, and the uncertainty in the input scale in quadrature, we obtain at

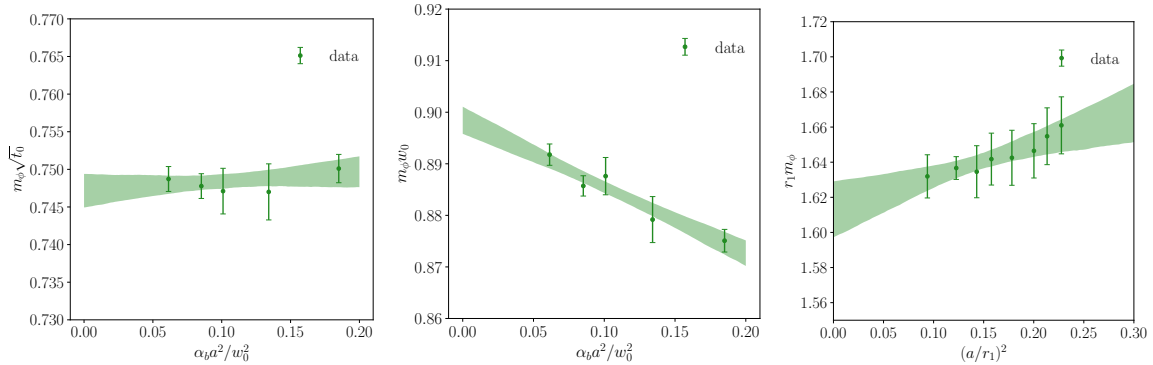


Figure 9. Continuum extrapolation of $m_\phi\sqrt{t_0}$ (left), $m_\phi w_0$ (middle) and $m_\phi r_1$ (right).

the final values for the gradient flow scales determined from the meson decay constants:

$$\begin{aligned}
 \sqrt{t_0} &= 0.14354 \text{ (99) fm, via } f_{\eta_s}, \\
 \sqrt{t_0} &= 0.14443 \text{ (83) fm, via } f_K, \\
 w_0 &= 0.17315 \text{ (129) fm, via } f_{\eta_s}, \\
 w_0 &= 0.17425 \text{ (89) fm, via } f_K.
 \end{aligned}
 \tag{4.2}$$

We see that the values of the gradient flow scales determined from f_{η_s} and f_K are consistent within errors. The above results on the gradient flow scales based on the pseudo-scalar meson decay constants are consistent with those determined via bottomonium mass splittings Eq (4.1) and the FLAG average [24].

Similarly, we determine the r_1 scale from the decay constants. For this we use the r_1/a values determined in Ref. [10] for $\beta = 6.460, 6.515, 6.575, 6.740,$ and 6.88 . We note that here we have also used the results from $\beta = 6.460$ lattice from Ref. [10], that was not used in the determination of the gradient flow scales listed in Tab. 1. We perform the continuum extrapolations of the dimensionless products $r_1 f_K$ and $r_1 f_{\eta_s}$ assuming linear dependence in $\alpha_b a^2/w_0^2$. The continuum extrapolation of $r_1 f_{\eta_s}$ and $r_1 f_K$ are shown in Fig. 8. To estimate the systematic uncertainty of the continuum extrapolation we perform extrapolation with and without the data with the largest lattice spacing corresponding to $\beta = 6.460$, and use the corresponding difference as the systematic error. The values for r_1 together with different sources of uncertainties are summarized in Tab. 5. Combining the different uncertainties in quadrature we obtain:

$$\begin{aligned}
 r_1 &= 0.3105 \text{ (43) fm, via } f_{\eta_s}, \\
 r_1 &= 0.3131 \text{ (40) fm, via } f_K.
 \end{aligned}
 \tag{4.3}$$

The values of r_1 obtained from f_K and f_{η_s} agree with each other as well with the value of r_1 obtained from the bottomonium splitting.

4.3 Scale determination through the ϕ meson mass

As a final check of our scale determination, we use the ϕ -meson mass, m_ϕ . Using m_ϕ to set the scale may not sound to be ideal since the ϕ meson is a resonance. However, its width is

only about 4 MeV, i.e. 0.4% of its mass. Therefore, we may expect that the errors of not treating the ϕ meson as a resonance should result in 0.4% error or less, which is smaller than the other sources of errors in our analysis. Using the values of the ϕ meson mass from Ref. [10] we performed continuum extrapolation for the products $\sqrt{t_0}m_\phi$ and w_0m_ϕ using the $\beta=6.423, 6.55, 6.664, 6.740$ and 6.88 lattices. We fit the above dimensionless combinations with $\alpha_b a^2/w_0^2$ -form. While the lattice results seem to follow the $\alpha_b a^2$ trend, the χ^2 of the fit appears to be large. We suspect that this is most likely due to the fact that the errors on the ϕ meson mass quoted in Ref. [10] are underestimated. Therefore, we rescale the errors on the ϕ meson mass by a factor of 2.5 before performing the $\alpha_b a^2/w_0^2$ extrapolations. Then the continuum extrapolations of $\sqrt{t_0}m_\phi$ and w_0m_ϕ have $\chi^2/\text{d.o.f.}$ around 1. The corresponding continuum extrapolations are shown in Fig. 9. To estimate the systematic uncertainties of the continuum extrapolation we perform extrapolations with both including and excluding the data for the largest lattice spacing corresponding to $\beta = 6.423$, and treating the corresponding difference as the systematic error. Finally we need to consider the error from the input scale. We will use the width of the ϕ meson of 4.25 MeV [60] as the error on the input scale instead of the error of its mass for the reasons explained above. The values of t_0 and w_0 in physical units obtained from the ϕ meson mass are shown in Tab. 5, where we also indicate various sources of errors.

To obtain the r_1 scale we consider product r_1m_ϕ using the lattice results for $\beta=6.423, 6.460, 6.488, 6.550, 6.608, 6.664, 6.740$ and 6.88 . We again perform the continuum extrapolations using the $\alpha_b a^2/w_0^2$ form of r_1m_ϕ . The $\chi^2/\text{d.o.f.}$ of the fits is close to one. To estimate the systematic errors of the continuum extrapolations we have performed fits with and without the coarsest lattice corresponding to $\beta = 6.423$. The value of r_1 in physical units obtained from the ϕ meson mass is shown in Tab. 5, including the various sources of errors.

Using the results for t_0 , w_0 and r_1 from Tab. 5 and combining the different sources of uncertainties as in the previous subsection, we arrive at the final values of the theory scales determined from the ϕ -meson mass

$$\begin{aligned}\sqrt{t_0} &= 0.14461 \text{ (80) fm, via } m_\phi, \\ w_0 &= 0.17389 \text{ (78) fm, via } m_\phi, \\ r_1 &= 0.3122 \text{ (33) fm, via } m_\phi,\end{aligned}\tag{4.4}$$

which agree well with other extractions.

4.4 Final values of the theory scales

To obtain the final values of the gradient flow scales we perform weighted average over the determinations via bottomonium mass splittings given by Eq. (4.1), the determinations via pseudo-scalar meson decay constants, f_K and f_{η_s} given by Eq. (4.2) and the determinations via the ϕ meson mass given by Eq. (4.4). We find:

$$\begin{aligned}\sqrt{t_0} &= 0.14428 \text{ (48) fm,} \\ w_0 &= 0.17391 \text{ (52) fm.}\end{aligned}\tag{4.5}$$

In Fig. 10 we compare our results on the gradient flow scales with the lattice results reviewed by FLAG 2024 report [24] both in 2+1 flavor QCD and in 2+1+1 flavor QCD as well as

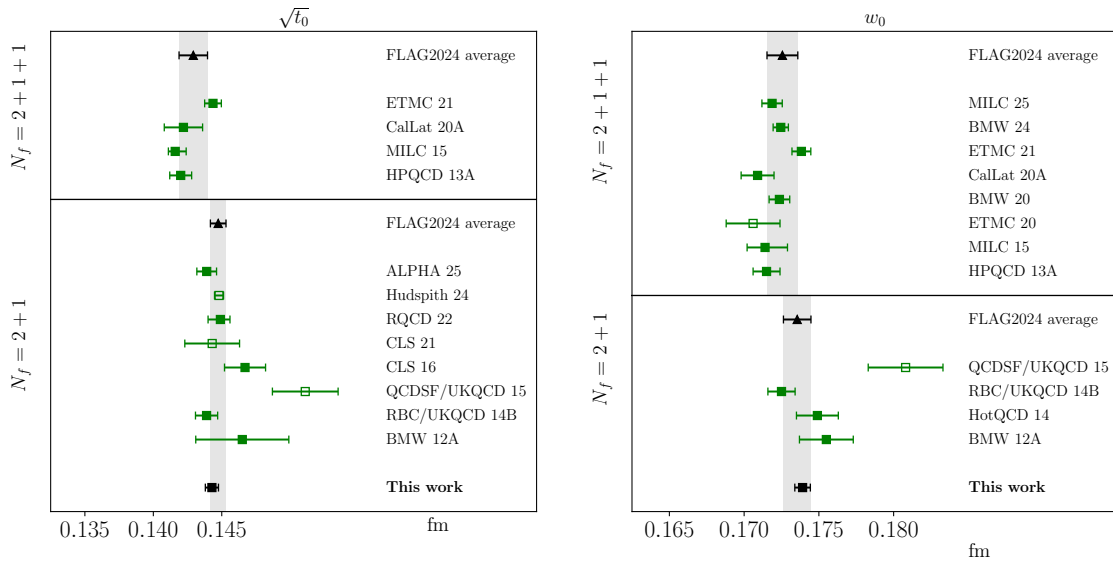


Figure 10. A comparison of the gradient-flow scales $\sqrt{t_0}$ (left) and w_0 (right) determined in this work with results from the literature included in FLAG 2024 review [24], as well as several recent determinations [23, 61, 62]. The literature results for $\sqrt{t_0}$ shown here include: ETMC 21 [15], CalLat 20A [2], MILC 15 [14], HPQCD 13A [18], ALPHA 25 [62], Hudspith 24 [63], RQCD 22 [64], CLS 21 [65], CLS 16 [17], QCDSF/UKQCD 15 [19], RBC/UKQCD 14B [1], and BMW 12A [3]. The literature results for w_0 shown here include: MILC 25 [23], BMW 24 [61], ETMC 21 [15], CalLat 20A [2], BMW 20 [16], ETMC 20 [66], MILC 15 [14], HPQCD 13A [18], QCDSF/UKQCD 15 [19], RBC/UKQCD 14B [1], HotQCD 14 [10], and BMW 12A [3].

with two recent determinations by BMW collaboration [61] (BMW 24) and Fermilab-MILC collaboration [23] (MILC 25) in 2+1+1 flavor QCD, and a very recent determination in 2+1 flavor QCD by ALPHA collaboration [62] (ALPHA 25). Our results for the gradient flow scales agree with the 2+1 flavor FLAG 2024 average. Moreover, both the FLAG average of t_0 and the recent determination by the ALPHA collaboration indicate that the value of t_0 differs between 2+1 flavor QCD and 2+1+1 flavor QCD. Our results confirm this picture, see Fig. 10 (left). The difference in the w_0 values between 2+1 and 2+1+1 flavor QCD is less pronounced in the FLAG 2024 report. However, our value of w_0 is larger than the recent 2+1+1 flavor determinations [23, 61], as shown in Fig. 10 (right). This suggests that w_0 , like t_0 , is also different in 2+1 flavor QCD and 2+1+1 flavor QCD.

To obtain the final value of r_1 scale we need to consider the fact that the largest source of uncertainty for this scale obtained through f_K , f_{η_s} and m_ϕ in Tab. 5 comes from the error on the values of r_1/a , which is common to all three determinations shown in this table. Therefore, we first perform a weighted sub-average of the r_1 values in Tab. 5 using the second and the third errors from Tab. 5 added in quadrature to obtain the weights, which gives $r_1 = 0.3123(8)$ fm. Then we use the largest error of 0.0037 in Tab. 5 as the common error and combine it with the error of the above result. This results in sub-average $r_1 = 0.3123(38)$ fm from the combined determination through f_K , f_{η_s} and m_ϕ . Using the weighted average of this result with the r_1 value obtained from bottomonium splitting and

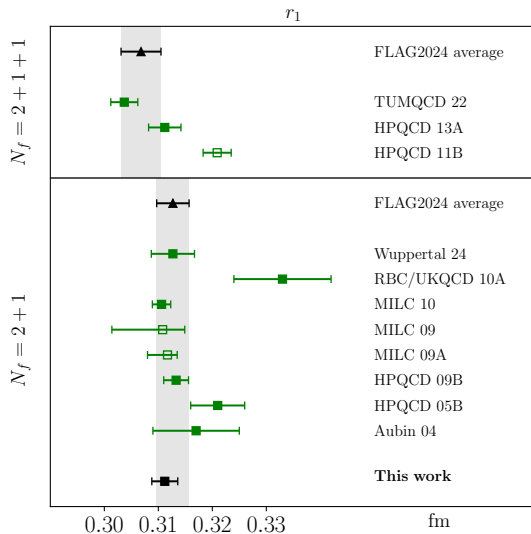


Figure 11. A comparison of the r_1 scales determined in this work with those included in the FLAG 2024 review [24], together with the recent determination of Ref. [35]. The literature values shown include results from TUMQCD 22 [12], HPQCD 13A [18], HPQCD 11B [57], Wuppertal 24 [35], RBC/UKQCD 10A [4], MILC 10 [67], MILC 09 [68], MILC 09A [69], HPQCD 09B [6], HPQCD 05B [56], and Aubin 04 [70].

given by Eq. (4.1) we obtain our final result for r_1 scale

$$r_1 = 0.3112(24) \text{ fm.} \quad (4.6)$$

Our final result on the r_1 scale is compared with other results from the literature in Fig. 11, including the recent value from Ref. [35] (Wuppertal 24). Our result agrees with most other lattice determinations in 2+1 flavor QCD, including that of Ref. [35], as shown in Fig. 11. It is in excellent agreement with the MILC collaboration’s value, $r_1 = 0.3106(18)$ fm [67], which was used to set the lattice spacing in the HotQCD studies. On the other hand, it is larger than the recent 2+1+1 flavor determination by the TUMQCD collaboration [12]. This may suggest that, similar to the gradient flow scales, the r_1 scale is influenced by the presence of the dynamical charm quark. To further investigate this, we use our continuum-extrapolated value of $r_1/\sqrt{t_0}$ from Eq. (3.3) together with the recent determination $\sqrt{t_0} = 0.1442(6)(4)$ fm from $f_{\pi K}$ [62]. This yields $r_1 = 0.3111(20)$ fm for 2+1 flavor QCD, in good agreement with our final result. Likewise, using the continuum-extrapolated value of r_1/w_0 in 2+1+1 flavor QCD from Eq. (3.4) and the recent determination $w_0 = 0.17187(96)$ fm obtained by the Fermilab–MILC collaboration from the Ω -baryon mass [23], we find $r_1 = 0.3044(16)$ fm, which agrees very well with the result from TUMQCD $r_1 = 0.3037(25)$ [12]. These considerations further support the conclusion that the values of r_1 differ between 2+1 flavor QCD and 2+1+1 flavor QCD.

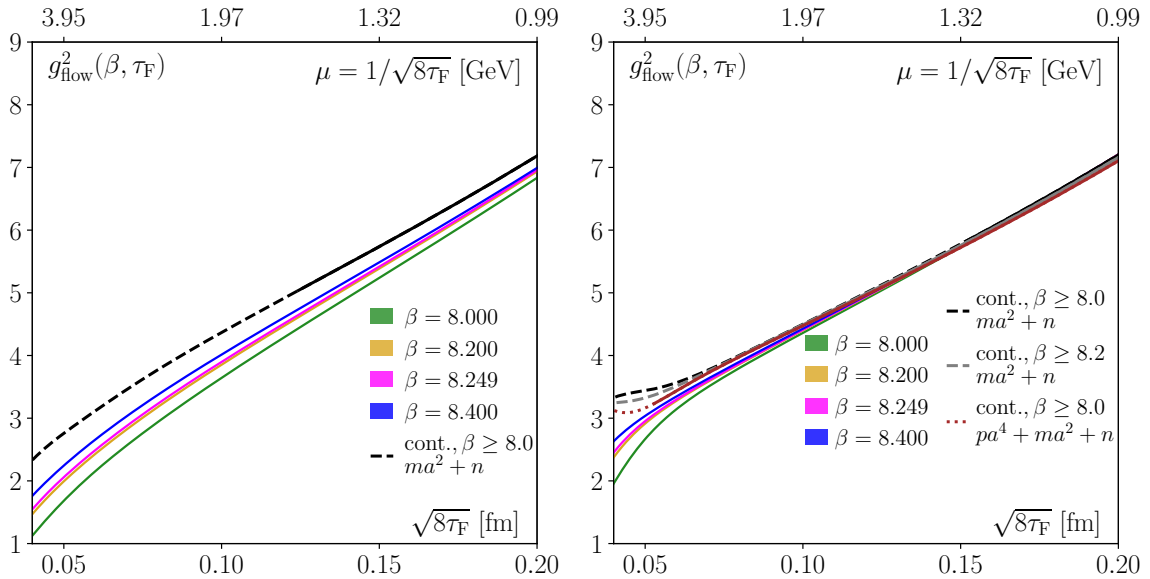


Figure 12. Left: the strong coupling in the gradient flow scheme measured using the clover discretization at finite lattice spacings (colored curves) and the continuum extrapolation of it using an Ansatz linear in a^2 (black curve). The dashed line type indicates that at the corresponding flow times the $\chi^2/\text{d.o.f.}$ of the continuum extrapolation is larger than 1.5. Right: same as the left but for the improved discretization. We also consider another Ansatz including a term quartic in a , which can describe the data in a much wider flow time range and try continuum extrapolation using different lattices. In these figures, the statistical errors are too small so we do not show them.

5 Gradient flow coupling

The action density in Eq. (2.6) that is used to define the gradient flow scales, t_i and w_i , can be calculated in perturbation theory when the flow time is sufficiently small. Therefore, the action density calculated with gradient flow can be used to define the gauge coupling in the gradient flow scheme (see e.g. [71, 72])

$$g_{\text{flow}}^2 = \frac{128\pi^2}{3(N_c^2 - 1)} \langle \tau_F^2 E \rangle, \quad (5.1)$$

where $N_c = 3$ for SU(3). This definition follows the same logic as the definition of the strong coupling from the static quark-antiquark potential or the corresponding force, see e.g. Ref. [73]. The gradient flow coupling is defined at some energy scale, μ_{flow} that is proportional to $1/\sqrt{\tau_F}$. Usually the definition $\mu_{\text{flow}} = 1/\sqrt{8\tau_F}$ is used. While the gradient flow coupling in Eq. (5.1) is defined for any τ_F , only for sufficiently small τ_F it can be related to other definitions of the coupling constant, e.g. to the conventionally used $\overline{\text{MS}}$ coupling. The relation between the gradient flow coupling and the $\overline{\text{MS}}$ coupling for $\mu_{\overline{\text{MS}}}^2 = \mu_{\text{flow}}^2$ can be written as

$$\alpha_{\text{flow}} \equiv \frac{g_{\text{flow}}^2}{4\pi} = \alpha_{\overline{\text{MS}}} (1 + k_1 \alpha_{\overline{\text{MS}}} + k_2 \alpha_{\overline{\text{MS}}}^2 + k_3 \alpha_{\overline{\text{MS}}}^3 + \dots). \quad (5.2)$$

The coefficients k_1 and k_2 have been calculated by Harlander and Neumann [74]

$$\begin{aligned} k_1 &= 1.098 + 0.008N_f, \\ k_2 &= -0.982 - 0.070N_f + 0.002N_f^2, \end{aligned} \tag{5.3}$$

while k_3 at present is unknown. In our case $N_f = 3$.

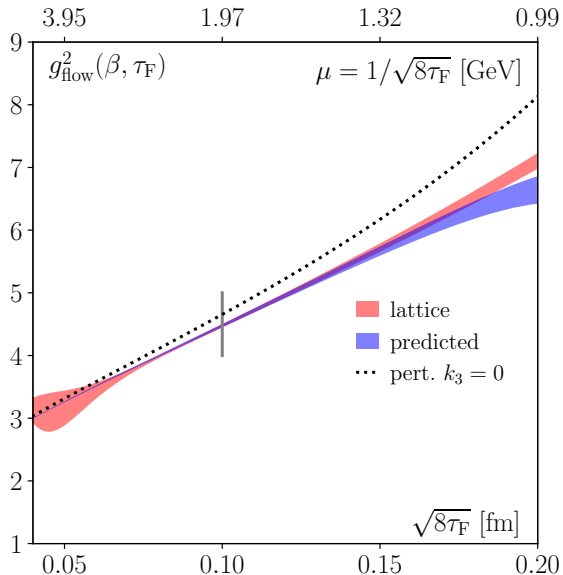


Figure 13. The gradient flow coupling obtained on the lattice compared with the perturbative prediction using $k_3 = 0$ and $k_3 = -1.7567$ (solved from Eq. (5.2) at $\sqrt{8\tau_F} = 0.1$ fm indicated by the vertical gray line), see text.

Our goal is to calculate the gradient flow coupling on the lattice in the continuum limit at small flow time, $\sqrt{8\tau_F} < 0.2$ fm and see to what extent the running of the gradient flow coupling can be described by perturbation theory. It turns out that lattice artifacts in the gradient flow coupling are quite large for $\sqrt{8\tau_F} < 0.2$ fm and continuum extrapolations are challenging. To minimize lattice artifacts when calculating the gradient flow coupling we only consider the highest four β values: 8.0, 8.2, 8.249 and 8.4. The gradient flow coupling calculated at these β values using the action density with the clover discretization and the improved discretization of the field strength tensor are shown in the left and right panels of Fig. 12, respectively. For clover discretization of the gauge action density we performed continuum extrapolation of g_{flow}^2 assuming a^2 -dependence, i.e. we performed fits using $ma^2 + n$ form. For $\sqrt{8\tau_F} < 0.12$ fm the fits had large $\chi^2/\text{d.o.f.}$, larger than 1.5. Thus for these τ_F values the continuum extrapolations are not reliable. From Fig. 12 (left) we see that lattice spacing dependence of g_{flow}^2 is significant and there is also a sizable difference between the continuum extrapolated value of gradient flow coupling and that obtained on the finest lattice. The situation is different for the improved discretization of the gauge action density as one can see in Fig. 12 (right). Namely, the dependence of the gradient flow coupling on β is much reduced. In the case of the improved discretization we performed different continuum extrapolations. We used simple quadratic form, $ma^2 + n$

form for continuum extrapolations and including all $\beta \geq 8.0$ lattices, or excluding the $\beta = 8.0$ lattice, or using quadratic plus quartic form, i.e. $pa^4 + ma^2 + n$ form for continuum extrapolations and using all $\beta \geq 8.0$ data. The corresponding continuum extrapolations are also shown in Fig. 12 (right). For $\sqrt{8\tau_F} > 0.075$ fm the difference between different continuum extrapolations is small. Furthermore, from Fig. 12 (right) we also see that the difference between the continuum extrapolated result and the result obtained on the finest lattice is also much smaller for improved discretization.

Since the continuum-extrapolated result for the gradient flow coupling was obtained from lattices with $\beta \geq 8.0$ where the light quark masses are heavier than the physical ones, the sensitivity of the gradient flow coupling to the light quark mass should be studied. In addition, the impact of frozen topology needs to be addressed. However, because our analysis focuses on the gradient flow coupling at relatively small flow times, the influence of frozen topology is expected to be minor. This expectation is confirmed in Appendix B, where a comparison of the flow-time dependence of g_{flow}^2 across different topological sectors shows that the differences remain negligible up to $\sqrt{8\tau_F} = 0.2$ fm. To investigate the effect of light-quark masses on the gradient flow coupling, we examine results on a slightly coarser lattice corresponding to $\beta = 7.825$, where simulations are available for two mass ratios, $m_s/m_l = 20$ and $m_s/m_l = 5$. As demonstrated in Appendix B, the differences in g_{flow}^2 between these two ensembles are very small, smaller than the uncertainty of the continuum extrapolation. Thus, at the current level of precision, the dependence on the light-quark masses can be neglected.

Having obtained continuum-extrapolated results for the gradient flow coupling, and having established that the effects of the light-quark mass and frozen topology can be neglected, we can now ask to what extent the flow-time dependence of g_{flow}^2 can be described by perturbation theory. Using the value $\Lambda_{\overline{\text{MS}}}^{N_f=3} = 338(10)$ MeV from FLAG 2024 [24], based on Refs. [52, 53, 75–82], and Eq. (5.2) with $k_3 = 0$, we obtain the perturbative prediction for the gradient flow coupling. This is shown in Fig. 13, together with the continuum-extrapolated lattice result whose uncertainty band includes both statistical and systematic contributions added in quadrature. The systematic uncertainty, arising from the continuum extrapolation, is taken as the larger of the two deviations shown in the right panel of Fig. 12: the difference between the black and brown curves, and the difference between the gray and brown curves.

A significant discrepancy is observed between the known perturbative result and the lattice data on the gradient flow coupling for $\sqrt{8\tau_F} > 0.075$ fm, likely due to the absence of higher-order terms in Eq. (5.2). To test this, we allow k_3 to be non-zero and fix its value by requiring that the perturbative expression in Eq. (5.2) reproduce the lattice result at $\sqrt{8\tau_F} = 0.1$ fm. This flow time is chosen because it is small enough for perturbation theory to be applicable, yet not so small that lattice errors dominate. The matching yields $k_3 = -1.7567$, which is larger in magnitude than k_1 or k_2 but still of comparable size. With this value of k_3 , the perturbative expression for g_{flow}^2 provides a reasonably good description of the lattice data up to $\sqrt{8\tau_F} = 0.15$ fm. This suggests that, once higher-order corrections are considered, perturbation theory can describe the running of the gradient flow coupling

up to this flow-time range.

An alternative way to explore to what extent perturbation theory can describe the running of the gradient flow coupling is to determine $\Lambda_{\overline{\text{MS}}}^{N_f=3}$ using our continuum extrapolated lattice data and Eq. (5.2). When doing so for $0.075 \text{ fm} \leq \sqrt{8\tau_F} \leq 0.15 \text{ fm}$ we find that $\Lambda_{\overline{\text{MS}}}^{N_f=3}$ lies in the range [300.9, 317.4] MeV. We will retain only the central value of the obtained range, 309.1 MeV, and disregard the variation stemming from the choice of τ_F . This is because, in the subsequent analysis, we will systematically evaluate all conceivable uncertainties in this calculation, including those related to missing higher-order perturbative corrections, which inherently subsume the uncertainty addressed here. We consider three sources: i) Statistical uncertainty: This is calculated using bootstrap resampling. ii) Systematic effects from continuum extrapolations: We exclude the coarsest lattice at $\beta = 8.0$ in the continuum extrapolation and take the difference from using the complete set of lattices as the systematic uncertainty. iii) Higher order perturbative terms in the conversion equation Eq. (5.2): To probe these effects we add a 3 loop term $k_3\alpha_{\overline{\text{MS}}}^3$ in Eq. (5.2), where $k_3 = 2k_2$ or $k_3 = -2k_2$. The difference from not having such a term will be quoted as another systematic uncertainty. All three error analyses are conducted at $\tau_F = 0.0816 \text{ fm}$, which corresponds to the maximum of the solved $\Lambda_{\overline{\text{MS}}}^{N_f=3}$. Collecting all the pieces we obtain

$$\Lambda_{\overline{\text{MS}}}^{N_f=3} = 309.1_{-0.7-5.0-11.6}^{+0.7+5.0+33.9} \text{ MeV}. \quad (5.4)$$

Our central value for the Λ parameter is lower than the FLAG average. However, it is still compatible with it within the estimated uncertainties. Very recently the ALPHA collaboration reported $\Lambda_{\overline{\text{MS}}} = 343.9(8.4)$ [83], which agrees with the above result within errors. Using the $\Lambda_{\overline{\text{MS}}}^{N_f=3}$ obtained above, for completeness we also compute $\alpha_{\overline{\text{MS}}}^{(5)}(M_Z)$ at the Z -boson mass by employing the decoupling relation between the strong coupling and the quark masses. This involves incrementally increasing the number of active quark flavors, starting from 3. The calculation is performed using the runDec function `crd.DecAsUpMS` with the following parameters: the $\overline{\text{MS}}$ charm quark mass at its own scale $m_{\text{charm}}=1.275 \text{ GeV}$, the $\overline{\text{MS}}$ bottom quark mass at its own scale $m_{\text{bottom}}=4.203 \text{ GeV}$, the Z -boson mass $M_Z=91.1876 \text{ GeV}$, and 5-loop accuracy. The result of this computation is $\alpha_{\overline{\text{MS}}}^{(5)}(M_Z) = 0.1161_{-0.0016}^{+0.0027}$, consistent with the FLAG-2024 average of $0.1183(7)$ [24] within the quoted errors.

6 Conclusions

In this paper we determined the gradient flow scales t_0 , w_0 , t_2 and w_2 in 2+1 flavor QCD using HISQ action in a wide range of lattice spacing. This allows us to use these scales to set the lattices spacing in the high temperature calculations performed by HotQCD collaboration. The physical values of t_0 and w_0 have been primarily determined using bottomonium splitting as an input. In addition, as a consistency check we also performed determination of these scales using f_K , f_{η_s} and the ϕ meson mass. performing a weighted average of these determinations we obtain: $\sqrt{t_0} = 0.14428(48) \text{ fm}$ and $w_0 = 0.17391(52) \text{ fm}$ as our final result. These values agree well with other lattice determinations in 2+1 flavor QCD, but are larger than the recent determinations in 2+1+1 flavor QCD, confirming

earlier expectations that the gradient flow scales are affected by the dynamical charm quark. We also revisited the determination of the r_1 scale from the heavy quark potential. We find $r_1 = 0.3112(24)$ fm, which agrees with other lattice QCD determinations in 2+1 flavor QCD but is larger than the recent determination of r_1 in 2+1+1 flavor QCD by TUMQCD collaboration [12]. This implies that also the r_1 scale is affected by the dynamical charm quark. Furthermore, we determined the ratios of the gradient flow scales and r_1 scale, which supports the above assertion.

Finally, we determined the gradient flow coupling in the continuum limit for small flow time. We find that it can be described by perturbation theory up to flow time $\sqrt{8\tau_F} = 0.15$ fm within the uncertainties.

Acknowledgements

This material is based upon work supported by The U.S. Department of Energy, Office of Science, Office of Nuclear Physics through Contract No. DE-SC0012704, within the frameworks of Scientific Discovery through Advanced Computing (SciDAC) award Fundamental Nuclear Physics at the Exascale and Beyond, and with "Heavy Flavor Theory for QCD Matter (HEFTY)" topical collaboration in Nuclear Theory. R.L. was supported by the Ministry of Culture and Science of the State of Northrhine Westphalia (MKW NRW) under the funding code NW21-024-A (NRW-FAIR). J.H.W.'s research has been funded by the Deutsche Forschungsgemeinschaft (DFG, German Research Foundation)—Projektnummer 417533893/GRK2575 Rethinking Quantum Field Theory. J.H.W. acknowledges the support by the State of Hesse within the Research Cluster ELEMENTS (Project ID 500/10.006).

This research used awards of computer time provided by the National Energy Research Scientific Computing Center (NERSC), a U.S. Department of Energy Office of Science User Facility located at Lawrence Berkeley National Laboratory, operated under Contract No. DE-AC02-05CH11231. Computations for this work were carried out in part on facilities of the USQCD Collaboration, which are funded by the Office of Science of the U.S. Department of Energy.

All computations in this work were performed using SIMULATEqCD [84–86].

Appendix

A Gradient flow scales computed on the finite lattices

In Tab. 6 and 7 we summarize the flow scales in lattice units $\sqrt{t_i}/a$ and w_i/a calculated on the ensembles listed in Tab. 1 using both clover and improved discretization.

B Influence of topological freezing and the light quark mass on flow observables

For $\beta \geq 8.0$ the topological charge, Q is frozen during Monte-Carlo sampling. For $\beta = 8.0, 8.2$ and 8.4 we have three independent Monte-Carlo streams labeled as a,b and c, some of which

β	$(\sqrt{t_0}/a)_{\text{clo.}}$	$(\sqrt{t_0}/a)_{\text{imp.}}$	$(\sqrt{t_2}/a)_{\text{clo.}}$	$(\sqrt{t_2}/a)_{\text{imp.}}$	$(w_0/a)_{\text{clo.}}$	$(w_0/a)_{\text{imp.}}$	$(w_2/a)_{\text{clo.}}$	$(w_2/a)_{\text{imp.}}$
6.423	-	0.9464(2)	-	0.7125(1)	-	1.1042(4)	-	0.8946(3)
6.515	-	1.0393(2)	-	0.7730(1)	-	1.2196(5)	-	0.9937(4)
6.550	-	1.0781(2)	-	0.7989(1)	-	1.2689(6)	-	1.0344(4)
6.575	-	1.1050(3)	-	0.8175(1)	-	1.3009(7)	-	1.0613(5)
6.664	-	1.2087(3)	-	0.8896(2)	-	1.4360(3)	-	1.1660(6)
6.740	1.4203(3)	1.3045(3)	1.1037(1)	0.9570(1)	1.5577(6)	1.5451(7)	1.2658(4)	1.2626(4)
6.880	1.6037(5)	1.4975(4)	1.2328(2)	1.0939(2)	1.7920(12)	1.7835(12)	1.4545(7)	1.4563(7)
7.030	1.8259(5)	1.7298(5)	1.3891(2)	1.2593(2)	2.0730(13)	2.0674(13)	1.6832(8)	1.6883(8)
7.150	2.0217(8)	1.9334(7)	1.5276(4)	1.4056(3)	2.3159(21)	2.3121(22)	1.8826(13)	1.8893(14)
7.280	2.2636(13)	2.1831(13)	1.6076(5)	1.5841(4)	2.6203(36)	2.6178(37)	2.1302(15)	2.1380(16)
7.373	2.4549(19)	2.3799(19)	1.8320(7)	1.7244(7)	2.8575(48)	2.8558(50)	2.3258(27)	2.3341(27)
7.596	2.9847(28)	2.9218(30)	2.2048(12)	2.1116(12)	3.5194(73)	3.5193(72)	2.8653(40)	2.8740(44)
7.825	3.634(9)	3.586(7)	2.669(3)	2.591(3)	4.292(24)	4.304(19)	3.510(13)	3.524(11)

Table 6. The dimensionless gradient flow scales $\sqrt{t_i}/a$ and w_i/a determined from different discretization at different β for the $m_s/m_l = 20$ ensembles.

β	$(\sqrt{t_0}/a)_{\text{clo.}}$	$(\sqrt{t_0}/a)_{\text{imp.}}$	$(\sqrt{t_2}/a)_{\text{clo.}}$	$(\sqrt{t_2}/a)_{\text{imp.}}$	$(w_0/a)_{\text{clo.}}$	$(w_0/a)_{\text{imp.}}$	$(w_2/a)_{\text{clo.}}$	$(w_2/a)_{\text{imp.}}$
7.030	1.806(3)	1.711(3)	1.380(1)	1.252(1)	2.022(5)	2.015(5)	1.652(4)	1.656(4)
7.825	3.622(9)	3.568(8)	2.664(4)	2.587(3)	4.262(19)	4.261(18)	3.486(14)	3.502(13)
8.000	4.228(33)	4.184(33)	3.096(12)	3.027(11)	4.978(83)	4.978(83)	4.083(47)	4.089(47)
8.200	5.083(79)	5.044(78)	3.688(21)	3.629(20)	6.156(345)	6.156(345)	4.999(188)	5.006(189)
8.249	5.262(50)	5.225(50)	3.837(26)	3.780(25)	6.233(81)	6.233(81)	5.109(60)	5.115(60)
8.400	6.076(108)	6.045(106)	4.399(32)	4.347(29)	7.293(330)	7.297(333)	5.954(199)	5.962(201)

Table 7. Same as Tab. 6 but for the $m_s/m_l = 5$ ensembles.

have differed values of Q . In Tab. 8 and in Fig. 14 we show the gradient flow scales for different streams. As one can see there is no statistically significant difference between the gradient flow scales corresponding to different values of Q . In Fig. 15 we show the gradient flow coupling as function of $\sqrt{8\tau_F}$ for different streams. While we see some differences in the value of the gradient flow coupling for large flow times, the results obtained from different streams agree for $\sqrt{8\tau_F} < 0.2$ fm, which is the focus of the present study. So our analysis of the gradient flow coupling is not affected by topological freezing.

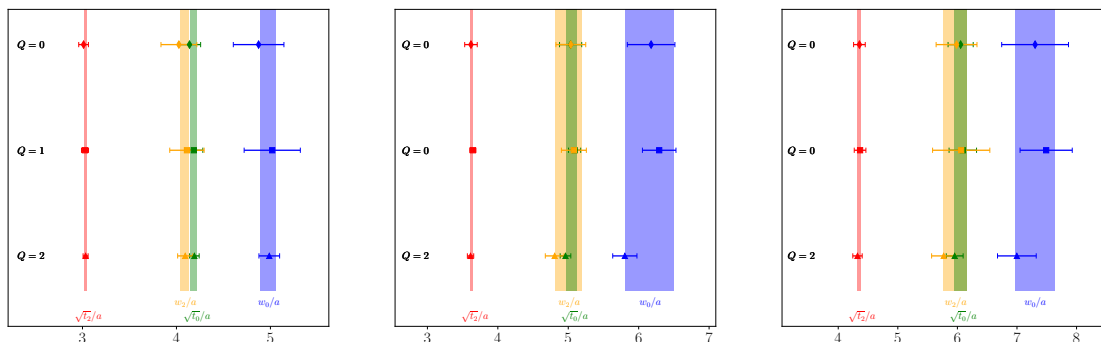


Figure 14. The gradient flow scales in lattice units $\sqrt{t_i}/a$ and w_i/a determined from the improved discretization at $\beta = 8.0$ (left), 8.2 (middle), 8.4 (right) in the different topological sectors. The mean and error for each stream are estimated from the original configurations instead of the binned ones, because the latter has only ~ 10 - 30 statistics for each stream. The bands denote the average over different streams, estimated from the bootstrap samples drawn from the binned configurations.

In Fig. 16 we show the gradient flow coupling for $\beta = 7.825$ for two values of the light quark mass. As one can see from the figure the mass effects are very small, smaller than

β	8.000			
	steam a	steam b	stream c	
	$Q = 2$	$Q = 1$	$Q = 0$	average
$\sqrt{t_0}/a(\text{impr.})$	4.191(51)	4.185(96)	4.139(118)	4.184(33)
$\sqrt{t_2}/a(\text{impr.})$	3.033(27)	3.027(37)	3.012(52)	3.027(11)
$w_0/a(\text{impr.})$	4.988(110)	5.019(299)	4.875(269)	4.978(83)
$w_2/a(\text{impr.})$	4.093(80)	4.112(183)	4.026(191)	4.089(47)
β	8.200			
	steam a	steam b	stream c	
	$Q = 2$	$Q = 1$	$Q = 0$	average
$\sqrt{t_0}/a(\text{impr.})$	4.961(76)	5.090(86)	5.034(158)	5.044(78)
$\sqrt{t_2}/a(\text{impr.})$	3.612(45)	3.645(43)	3.618(89)	3.629(20)
$w_0/a(\text{impr.})$	5.804(172)	6.291(238)	6.177(338)	6.156(345)
$w_2/a(\text{impr.})$	4.807(133)	5.080(177)	5.037(212)	5.006(189)
β	8.400			
	steam a	steam b	stream c	
	$Q = 2$	$Q = 1$	$Q = 0$	average
$\sqrt{t_0}/a(\text{impr.})$	5.955(142)	6.091(231)	6.054(211)	6.045(106)
$\sqrt{t_2}/a(\text{impr.})$	4.323(79)	4.367(98)	4.356(98)	4.347(29)
$w_0/a(\text{impr.})$	6.998(325)	7.490(438)	7.304(561)	7.297(333)
$w_2/a(\text{impr.})$	5.770(203)	6.064(480)	5.986(343)	5.962(201)

Table 8. The gradient flow scales $\sqrt{t_i}/a$ and w_i/a in lattice units determined from the improved discretization at different $\beta = 8.0, 8.2, 8.4$ in the different topological sectors.

the uncertainties in the continuum extrapolation. Thus, we can use the $m_s/m_l = 5$ lattice results to perform comparison with perturbation theory.

References

- [1] T. Blum *et al.* (RBC, UKQCD), *Phys. Rev. D* **93**, 074505 (2016), [arXiv:1411.7017 \[hep-lat\]](#) .
- [2] N. Miller *et al.*, *Phys. Rev. D* **103**, 054511 (2021), [arXiv:2011.12166 \[hep-lat\]](#) .
- [3] S. Borsányi, S. Dürr, Z. Fodor, C. Hoelbling, S. D. Katz, S. Krieg, T. Kurth, L. Lellouch, T. Lippert, and C. McNeile (BMW), *JHEP* **09**, 010 (2012), [arXiv:1203.4469 \[hep-lat\]](#) .
- [4] Y. Aoki *et al.* (RBC, UKQCD), *Phys. Rev. D* **83**, 074508 (2011), [arXiv:1011.0892 \[hep-lat\]](#) .
- [5] S. Aoki *et al.* (PACS-CS), *Phys. Rev. D* **79**, 034503 (2009), [arXiv:0807.1661 \[hep-lat\]](#) .
- [6] C. T. H. Davies, E. Follana, I. D. Kendall, G. P. Lepage, and C. McNeile (HPQCD), *Phys. Rev. D* **81**, 034506 (2010), [arXiv:0910.1229 \[hep-lat\]](#) .
- [7] R. Sommer, *Nucl. Phys. B* **411**, 839 (1994), [arXiv:hep-lat/9310022](#) .
- [8] C. W. Bernard, T. Burch, K. Orginos, D. Toussaint, T. A. DeGrand, C. E. DeTar, S. A. Gottlieb, U. M. Heller, J. E. Hetrick, and B. Sugar, *Phys. Rev. D* **62**, 034503 (2000), [arXiv:hep-lat/0002028](#) .

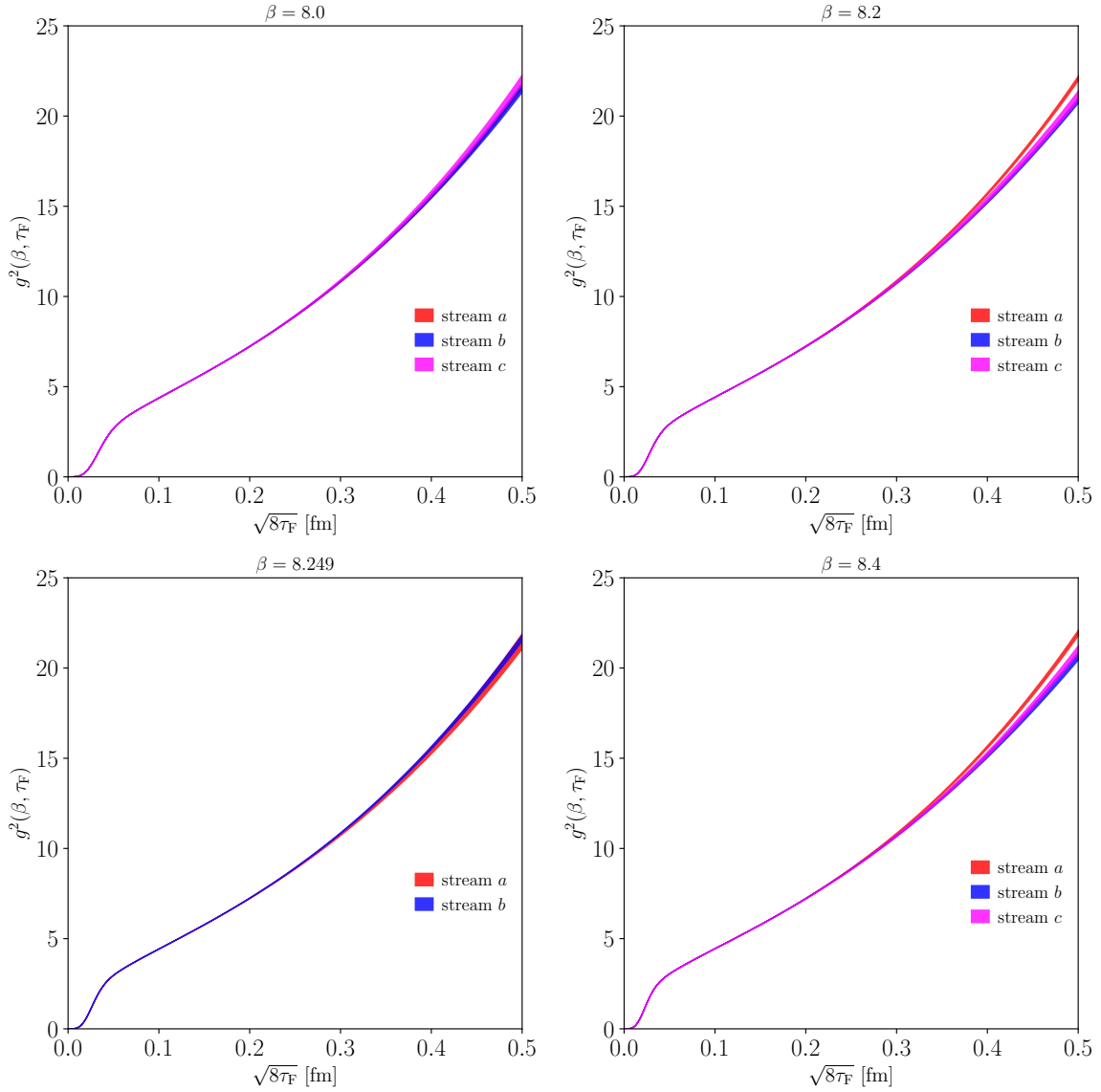


Figure 15. g_{flow}^2 as function of flow time for different streams.

- [9] A. Francis, O. Kaczmarek, M. Laine, T. Neuhaus, and H. Ohno, *Phys. Rev. D* **91**, 096002 (2015), [arXiv:1503.05652 \[hep-lat\]](#) .
- [10] A. Bazavov *et al.* (HotQCD), *Phys. Rev. D* **90**, 094503 (2014), [arXiv:1407.6387 \[hep-lat\]](#) .
- [11] A. Bazavov *et al.*, *Phys. Rev. D* **85**, 054503 (2012), [arXiv:1111.1710 \[hep-lat\]](#) .
- [12] N. Brambilla, R. L. Delgado, A. S. Kronfeld, V. Leino, P. Petreczky, S. Steinbeißer, A. Vairo, and J. H. Weber (TUMQCD), *Phys. Rev. D* **107**, 074503 (2023), [arXiv:2206.03156 \[hep-lat\]](#) .
- [13] A. Bazavov *et al.* (MILC), *Phys. Rev. D* **87**, 054505 (2013), [arXiv:1212.4768 \[hep-lat\]](#) .
- [14] A. Bazavov *et al.* (MILC), *Phys. Rev. D* **93**, 094510 (2016), [arXiv:1503.02769 \[hep-lat\]](#) .
- [15] C. Alexandrou *et al.* (Extended Twisted Mass), *Phys. Rev. D* **104**, 074520 (2021),

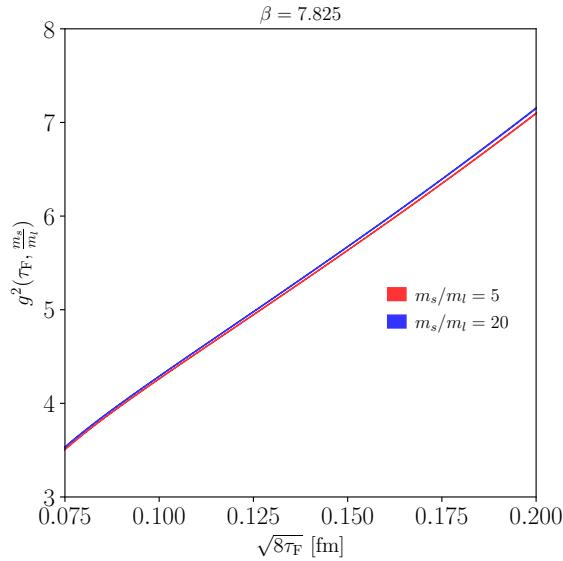


Figure 16. Comparison of the gradient flow coupling obtained from $m_s/m_l = 5$ and from $m_s/m_l = 20$ at $\beta = 7.825$ for the improved discretization of the action.

[arXiv:2104.06747 \[hep-lat\]](#) .

- [16] S. Borsanyi *et al.*, *Nature* **593**, 51 (2021), [arXiv:2002.12347 \[hep-lat\]](#) .
- [17] M. Bruno, T. Korzec, and S. Schaefer, *Phys. Rev. D* **95**, 074504 (2017), [arXiv:1608.08900 \[hep-lat\]](#) .
- [18] R. J. Dowdall, C. T. H. Davies, G. P. Lepage, and C. McNeile, *Phys. Rev. D* **88**, 074504 (2013), [arXiv:1303.1670 \[hep-lat\]](#) .
- [19] V. G. Bornyakov *et al.*, (2015), [arXiv:1508.05916 \[hep-lat\]](#) .
- [20] R. Narayanan and H. Neuberger, *JHEP* **03**, 064 (2006), [arXiv:hep-th/0601210](#) .
- [21] M. Luscher, *Commun. Math. Phys.* **293**, 899 (2010), [arXiv:0907.5491 \[hep-lat\]](#) .
- [22] M. Luscher and P. Weisz, *JHEP* **02**, 051 (2011), [arXiv:1101.0963 \[hep-th\]](#) .
- [23] A. Bazavov *et al.*, (2025), [arXiv:2509.14367 \[hep-lat\]](#) .
- [24] Y. Aoki *et al.* (Flavour Lattice Averaging Group (FLAG)), (2024), [arXiv:2411.04268 \[hep-lat\]](#) .
- [25] A. Bazavov, P. Petreczky, and J. H. Weber, *Phys. Rev. D* **97**, 014510 (2018), [arXiv:1710.05024 \[hep-lat\]](#) .
- [26] L. Altenkort, O. Kaczmarek, R. Larsen, S. Mukherjee, P. Petreczky, H.-T. Shu, and S. Stendebach (HotQCD), *Phys. Rev. Lett.* **130**, 231902 (2023), [arXiv:2302.08501 \[hep-lat\]](#) .
- [27] A. Bazavov, H. T. Ding, P. Hegde, F. Karsch, C. Miao, S. Mukherjee, P. Petreczky, C. Schmidt, and A. Velytsky, *Phys. Rev. D* **88**, 094021 (2013), [arXiv:1309.2317 \[hep-lat\]](#) .
- [28] H. T. Ding, S. Mukherjee, H. Ohno, P. Petreczky, and H. P. Schadler, *Phys. Rev. D* **92**, 074043 (2015), [arXiv:1507.06637 \[hep-lat\]](#) .
- [29] A. Bazavov, N. Brambilla, H. T. Ding, P. Petreczky, H. P. Schadler, A. Vairo, and J. H. Weber, *Phys. Rev. D* **93**, 114502 (2016), [arXiv:1603.06637 \[hep-lat\]](#) .

- [30] A. Bazavov, N. Brambilla, P. Petreczky, A. Vairo, and J. H. Weber (TUMQCD), *Phys. Rev. D* **98**, 054511 (2018), [arXiv:1804.10600 \[hep-lat\]](#) .
- [31] L. Altenkort, D. de la Cruz, O. Kaczmarek, R. Larsen, G. D. Moore, S. Mukherjee, P. Petreczky, H.-T. Shu, and S. Stendebach (HotQCD), *Phys. Rev. Lett.* **132**, 051902 (2024), [arXiv:2311.01525 \[hep-lat\]](#) .
- [32] A. Bazavov, D. Horying, R. N. Larsen, S. Mukherjee, P. Petreczky, A. Rothkopf, and J. H. Weber (HotQCD), *Phys. Rev. D* **109**, 074504 (2024), [arXiv:2308.16587 \[hep-lat\]](#) .
- [33] H.-T. Ding, W.-P. Huang, R. Larsen, S. Meinel, S. Mukherjee, P. Petreczky, and Z. Tang, *JHEP* **05**, 149 (2025), [arXiv:2501.11257 \[hep-lat\]](#) .
- [34] D. Bollweg, J. L. Dasilva Golán, O. Kaczmarek, R. N. Larsen, G. D. Moore, S. Mukherjee, P. Petreczky, H.-T. Shu, S. Stendebach, and J. H. Weber (HotQCD), *JHEP* **09**, 180 (2025), [arXiv:2506.11958 \[hep-lat\]](#) .
- [35] T. M. B. Asmussen, R. Höllwieser, F. Knechtli, and T. Korzec, *Eur. Phys. J. C* **85**, 673 (2025), [arXiv:2412.10215 \[hep-lat\]](#) .
- [36] A. Hasenfratz, C. T. Peterson, J. van Sickle, and O. Witzel, *Phys. Rev. D* **108**, 014502 (2023), [arXiv:2303.00704 \[hep-lat\]](#) .
- [37] C. H. Wong, S. Borsanyi, Z. Fodor, K. Holland, and J. Kuti, *PoS LATTICE2022*, 043 (2023), [arXiv:2301.06611 \[hep-lat\]](#) .
- [38] A. Ramos and S. Sint, *Eur. Phys. J. C* **76**, 15 (2016), [arXiv:1508.05552 \[hep-lat\]](#) .
- [39] M. Luscher and P. Weisz, *Commun. Math. Phys.* **98**, 433 (1985), [Erratum: *Commun.Math.Phys.* 98, 433 (1985)].
- [40] M. Luscher and P. Weisz, *Phys. Lett. B* **158**, 250 (1985).
- [41] M. Lüscher, *JHEP* **08**, 071 (2010), [Erratum: *JHEP* 03, 092 (2014)], [arXiv:1006.4518 \[hep-lat\]](#) .
- [42] L. Altenkort, A. M. Eller, O. Kaczmarek, L. Mazur, G. D. Moore, and H.-T. Shu, *Phys. Rev. D* **103**, 014511 (2021), [arXiv:2009.13553 \[hep-lat\]](#) .
- [43] L. Altenkort, A. M. Eller, O. Kaczmarek, L. Mazur, G. D. Moore, and H.-T. Shu, *Phys. Rev. D* **103**, 114513 (2021), [arXiv:2012.08279 \[hep-lat\]](#) .
- [44] N. Brambilla, V. Leino, J. Mayer-Staudte, and P. Petreczky (TUMQCD), *Phys. Rev. D* **107**, 054508 (2023), [arXiv:2206.02861 \[hep-lat\]](#) .
- [45] L. Altenkort, A. M. Eller, A. Francis, O. Kaczmarek, L. Mazur, G. D. Moore, and H.-T. Shu, *Phys. Rev. D* **108**, 014503 (2023), [arXiv:2211.08230 \[hep-lat\]](#) .
- [46] S. Borsanyi, Z. Fodor, J. N. Guenther, S. D. Katz, P. Parotto, A. Pasztor, D. Pesznyak, K. K. Szabo, and C. H. Wong, *Phys. Rev. D* **110**, L011501 (2024), [arXiv:2312.07528 \[hep-lat\]](#) .
- [47] C. Gattringer and C. B. Lang, *Quantum chromodynamics on the lattice*, Vol. 788 (Springer, Berlin, 2010).
- [48] S. O. Bilson-Thompson, D. B. Leinweber, and A. G. Williams, *Annals Phys.* **304**, 1 (2003), [arXiv:hep-lat/0203008](#) .
- [49] C. R. Allton, *Nucl. Phys. B Proc. Suppl.* **53**, 867 (1997), [arXiv:hep-lat/9610014](#) .
- [50] E. Follana, Q. Mason, C. Davies, K. Hornbostel, G. P. Lepage, J. Shigemitsu, H. Trottier, and K. Wong (HPQCD, UKQCD), *Phys. Rev. D* **75**, 054502 (2007), [arXiv:hep-lat/0610092](#) .

- [51] P. Petreczky and J. H. Weber, *Phys. Rev. D* **100**, 034519 (2019), [arXiv:1901.06424 \[hep-lat\]](#) .
- [52] P. Petreczky and J. H. Weber, *Eur. Phys. J. C* **82**, 64 (2022), [arXiv:2012.06193 \[hep-lat\]](#) .
- [53] A. Bazavov, N. Brambilla, X. Garcia i Tormo, P. Petreczky, J. Soto, A. Vairo, and J. H. Weber (TUMQCD), *Phys. Rev. D* **100**, 114511 (2019), [arXiv:1907.11747 \[hep-lat\]](#) .
- [54] N. J. Brown, (2018), [10.7936/K7S181ZQ](#).
- [55] R. Larsen, S. Meinel, S. Mukherjee, and P. Petreczky, *Phys. Lett. B* **800**, 135119 (2020), [arXiv:1910.07374 \[hep-lat\]](#) .
- [56] A. Gray, I. Allison, C. T. H. Davies, E. Dalgic, G. P. Lepage, J. Shigemitsu, and M. Wingate, *Phys. Rev. D* **72**, 094507 (2005), [arXiv:hep-lat/0507013](#) .
- [57] R. J. Dowdall *et al.* (HPQCD), *Phys. Rev. D* **85**, 054509 (2012), [arXiv:1110.6887 \[hep-lat\]](#) .
- [58] M. Tanabashi *et al.* (Particle Data Group), *Phys. Rev. D* **98**, 030001 (2018).
- [59] S. Meinel, *Phys. Rev. D* **82**, 114502 (2010), [arXiv:1007.3966 \[hep-lat\]](#) .
- [60] S. Navas *et al.* (Particle Data Group), *Phys. Rev. D* **110**, 030001 (2024).
- [61] A. Boccaletti *et al.*, (2024), [arXiv:2407.10913 \[hep-lat\]](#) .
- [62] A. Bussone, A. Conigli, J. Frison, G. Herdoíza, C. Pena, D. Preti, J. Á. Romero, A. Sáez, and J. Ugarrío (ALPHA), (2025), [arXiv:2510.20450 \[hep-lat\]](#) .
- [63] R. J. Hudspith, M. F. M. Lutz, and D. Mohler, (2024), [arXiv:2404.02769 \[hep-lat\]](#) .
- [64] G. S. Bali, S. Collins, P. Georg, D. Jenkins, P. Korcyl, A. Schäfer, E. E. Scholz, J. Simeth, W. Söldner, and S. Weishäupl (RQCD), *JHEP* **05**, 035 (2023), [arXiv:2211.03744 \[hep-lat\]](#) .
- [65] B. Strassberger *et al.*, *PoS LATTICE2021*, 135 (2022), [arXiv:2112.06696 \[hep-lat\]](#) .
- [66] G. Bergner, P. Dimopoulos, J. Finkenrath, E. Fiorenza, R. Frezzotti, M. Garofalo, B. Kostrzewa, F. Sanfilippo, S. Simula, and U. Wenger (Extended Twisted Mass), *PoS LATTICE2019*, 181 (2020), [arXiv:2001.09116 \[hep-lat\]](#) .
- [67] A. Bazavov *et al.* (MILC), *PoS LATTICE2010*, 074 (2010), [arXiv:1012.0868 \[hep-lat\]](#) .
- [68] A. Bazavov *et al.* (MILC), *Rev. Mod. Phys.* **82**, 1349 (2010), [arXiv:0903.3598 \[hep-lat\]](#) .
- [69] A. Bazavov *et al.* (MILC), *PoS CD09*, 007 (2009), [arXiv:0910.2966 \[hep-ph\]](#) .
- [70] C. Aubin, C. Bernard, C. DeTar, J. Osborn, S. Gottlieb, E. B. Gregory, D. Toussaint, U. M. Heller, J. E. Hetrick, and R. Sugar, *Phys. Rev. D* **70**, 094505 (2004), [arXiv:hep-lat/0402030](#) .
- [71] Z. Fodor, K. Holland, J. Kuti, D. Negradi, and C. H. Wong, *JHEP* **11**, 007 (2012), [arXiv:1208.1051 \[hep-lat\]](#) .
- [72] A. Hasenfratz and O. Witzel, *Phys. Rev. D* **101**, 034514 (2020), [arXiv:1910.06408 \[hep-lat\]](#) .
- [73] S. Necco and R. Sommer, *Phys. Lett. B* **523**, 135 (2001), [arXiv:hep-ph/0109093](#) .
- [74] R. V. Harlander and T. Neumann, *JHEP* **06**, 161 (2016), [arXiv:1606.03756 \[hep-ph\]](#) .
- [75] C. McNeile, C. T. H. Davies, E. Follana, K. Hornbostel, and G. P. Lepage, *Phys. Rev. D* **82**, 034512 (2010), [arXiv:1004.4285 \[hep-lat\]](#) .
- [76] B. Chakraborty, C. T. H. Davies, B. Galloway, P. Knecht, J. Koponen, G. C. Donald, R. J. Dowdall, G. P. Lepage, and C. McNeile, *Phys. Rev. D* **91**, 054508 (2015), [arXiv:1408.4169 \[hep-lat\]](#) .

- [77] M. Dalla Brida, R. Höllwieser, F. Knechtli, T. Korzec, A. Nada, A. Ramos, S. Sint, and R. Sommer (ALPHA), *Eur. Phys. J. C* **82**, 1092 (2022), [arXiv:2209.14204 \[hep-lat\]](#) .
- [78] C. Ayala, X. Lobregat, and A. Pineda, *JHEP* **09**, 016 (2020), [arXiv:2005.12301 \[hep-ph\]](#) .
- [79] S. Cali, K. Cichy, P. Korcyl, and J. Simeth, *Phys. Rev. Lett.* **125**, 242002 (2020), [arXiv:2003.05781 \[hep-lat\]](#) .
- [80] M. Bruno, M. Dalla Brida, P. Fritzsche, T. Korzec, A. Ramos, S. Schaefer, H. Simma, S. Sint, and R. Sommer (ALPHA), *Phys. Rev. Lett.* **119**, 102001 (2017), [arXiv:1706.03821 \[hep-lat\]](#) .
- [81] S. Aoki *et al.* (PACS-CS), *JHEP* **10**, 053 (2009), [arXiv:0906.3906 \[hep-lat\]](#) .
- [82] K. Maltman, D. Leinweber, P. Moran, and A. Sternbeck, *Phys. Rev. D* **78**, 114504 (2008), [arXiv:0807.2020 \[hep-lat\]](#) .
- [83] M. D. Brida, R. Höllwieser, F. Knechtli, T. Korzec, A. Ramos, S. Sint, and R. Sommer, (2025), [arXiv:2501.06633 \[hep-ph\]](#) .
- [84] L. Mazur, *Topological Aspects in Lattice QCD*, *Ph.D. thesis*, Bielefeld U. (2021).
- [85] D. Bollweg, L. Altenkort, D. A. Clarke, O. Kaczmarek, L. Mazur, C. Schmidt, P. Scior, and H.-T. Shu, *PoS LATTICE2021*, 196 (2022), [arXiv:2111.10354 \[hep-lat\]](#) .
- [86] L. Mazur *et al.* (HotQCD), *Comput. Phys. Commun.* **300**, 109164 (2024), [arXiv:2306.01098 \[hep-lat\]](#) .